Optical Frequency Division by 3 Employing Self-Phase-Locking in Periodically Poled Lithium Niobate

by

Pavel Vladimir Gorelik

Submitted to the Department of Electrical Engineering and Computer Science
in partial fulfillment of the requirements for the degree of

Master of Engineering in Electrical Engineering

at the

MASSACHUSETTS INSTITUTE OF TECHNOLOGY

February 2005

Author .....
Department of Electrical Engineering and Computer Science
January 28, 2005

Certified by .....
Dr. Franco N. C. Wong
Senior Research Scientist
Thesis Supervisor

Accepted by .....
Arthur C. Smith
Chairman, Department Committee on Graduate Students

Optical Frequency Division By-3 Employing Self-Phase Locking in Periodically Poled Lithium Niobate

by

Pavel Vladimir Gorelik

Submitted to the Department of Electrical Engineering and Computer Science
on January 28, 2005, in partial fulfillment of the
requirements for the degree of
Master of Engineering in Electrical Engineering

Abstract

A method used to obtain frequencies in precise ratios of 2/3 and 1/3 of the pump is described as a possible way to extend the usable range of octave-spanning optical frequency combs for frequency metrology applications. The divider is based on a self-phase locked optical parametric oscillation in a doubly resonant semi-monolithic optical cavity containing a dual-grating periodically poled lithium niobate. The design, implementation and evaluation of such a frequency divider are described. Preliminary experimental data from the self-phase locked optical frequency divider is presented. We have obtained sub-100 mW threshold for the optical parametric oscillator with stable operation over 1 s without servo locking the cavity length. Preliminary results suggest that self-phase locking has been observed.

Thesis Supervisor: Dr. Franco N. C. Wong
Title: Senior Research Scientist

Acknowledgments

I express my gratitude to Dr. Franco Wong for introducing this field to me and being a mentor and a guide in terms of my theoretical understanding as well as my experimental skills. This work would not have been possible without the help and critique of all my co-workers and especially my office mate Chris Kuklewicz who helped clear up many problems. The work with Dr. J. J. Zondy and Dr. D. Kolker, at their Paris laboratory, was an invaluable experience that provided knowledge and experience with the behavioral intricacies of optical divider systems, and for that I am grateful. I also thank Grace Eichinger who, especially in the last months, has been a source of strength, confidence, and support.

Contents

List of Figures

List of Tables

Chapter 1

Background

1.1 The Need to Measure Optical Frequencies

The precise and accurate measurement of frequencies, or frequency metrology, is fundamentally important to the progress of science and technology. The definitions of standard units of time and length depend on a highly periodic event and an accurate method to determine its periodicity. Furthermore, technologies underlying modern communications, navigation, and measurement also depend on stable and accurate frequency standards and frequency measurement methods [1].

In physics and basic research optical frequency metrology is a corner-stone technology. Many of the methods used to study physical phenomena rely on spectral and time dependent measurements. Numerous examples can be found in astronomy, material science and atomic physics. Frequency metrology is also required to measure certain fundamental physical constants as well as their time dependence, and to confirm fundamental theories such as general relativity and quantum electrodynamics.

In commercial and engineering applications metrology is required in satellite navigation and ranging systems such as the global positioning system (GPS). Future deep space optical communication and telecommunication systems will also require highly accurate frequency standards and measurement systems.

The current primary frequency standard is a 9.2 GHz cesium atomic clock. Variations of this microwave standard have been in use during the last half century and

its accuracy and stability have improved by several orders of magnitude during this time. The longevity of this standard enabled it to be thoroughly tested and has produced a plethora of technologies tied directly to it. However, new secondary standards operating at optical frequencies, with better short term accuracies, have been demonstrated. Some of the new optical standards appear promising because their improved accuracies would allow advancements in basic and applied sciences, as well as in commercial applications. A more accurate frequency standard would allow physical quantities such as the Rydberg constant (currently known to one part in 10^{11} [2]) and the fine structure constant to be measured more accurately. More importantly, it would allow the time dependence of these "constants" to be evaluated. Furthermore, an improved standard may lead to redefinition of the SI units for time and length with better accuracies. It would also improve observation techniques such as long baseline interferometry and gravity wave detection, and enable new technologies with higher resolution, accuracy and signal-to-noise ratios to emerge. A better standard would also bring about advancements in telecommunications and navigation. In order to advance the existing technologies and to realize the new ones by taking advantage of the improved accuracies offered by various optical standards a method to accurately and directly measure optical frequencies is essential.

There is a problem with measuring frequencies far beyond the microwave range, however. Specifically, there are no counters at optical frequencies, which are 4 orders of magnitude higher than microwave frequencies, where the primary cesium standard is located. Current semiconductor devices that are at the bleeding edge of the state of the art can function near 100 GHz; however, visible optical frequencies are on the order of hundreds of THz.

Thus there are two problems that need to be addressed in the future. First, better clocks, with higher accuracies and stabilities than the current cesium standard need to be developed. Second, in order to measure optical frequencies and to be able to utilize optical frequency oscillations as a reference, an efficient method of bridging the frequency gap between microwave and optical frequencies is needed. A part of the challenge of building a system to bridge the frequency gap will be addressed in

this thesis; other challenges and an overview of their solutions are given in Appendix A.

1.2 Octave Spanning Mode-Locked Laser Frequency Combs

The most recent and widely accepted solution to bridge the gap between the microwave frequencies, where the primary standard is located, and optical frequencies is to use a frequency comb that is based on a femtosecond (fs) mode-locked laser [3]. The fs comb comprises an array of evenly spaced frequency markers spanning an octave or more in the optical frequency range. Such combs have been verified to be stable with no deviation from absolute periodicity within the experimental resolution of several parts in 10^{17} [4]. The carrier envelope frequency offset f_0 can be measured by utilizing a self referencing technique in which a nonlinear crystal is used to double one of the low frequency comb elements and performing a beat measurement against one of the higher frequency comb components. The beat frequency is in the microwave range and can be directly referenced to an atomic clock as shown in Figure 1-1.

Currently there are several "flavors" of this type of comb, the primary difference between them being the laser used, and therefore the wavelengths covered. The most frequently utilized comb uses a Ti:Sapphire laser and spans from $\lambda \approx 0.5\mu$ to $\lambda \approx 1.1\mu$; the Ti:Al_2O_3 has an ultrabroad gain bandwidth which makes it suitable for ultrashort-pulse mode-locked operation [5]. Combs have also been realized using Cr:forsterite and Cr:YAG lasers that cover longer wavelengths. Additionally, in some cases a microstructured fiber has been used to broaden out the spectrum [6], however this solution adds noise to the system and its use has diminished with the development of wide-band fiberless combs [7].

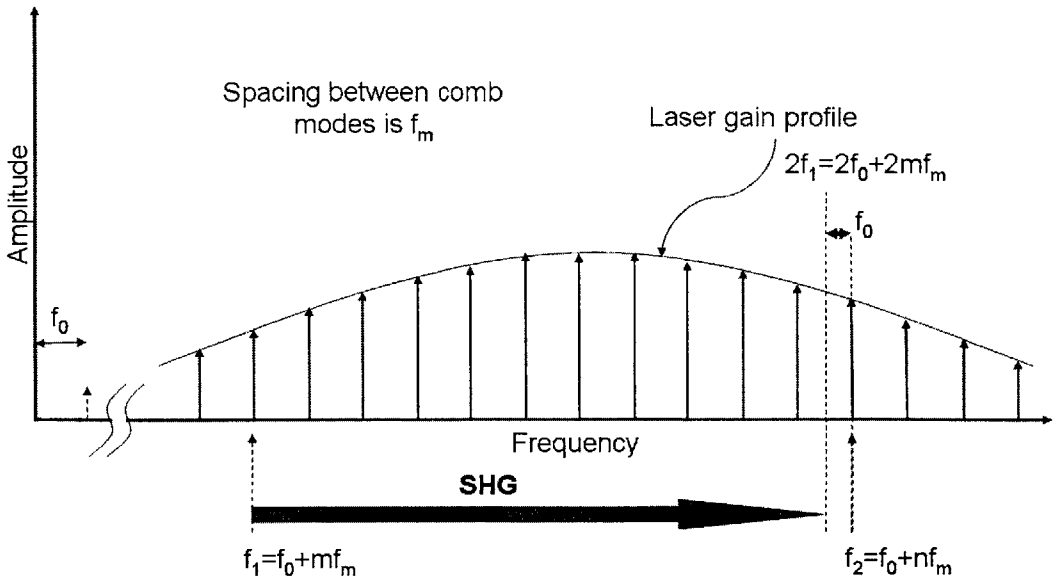

Figure 1-1: The carrier envelope offset frequency f_0 of the comb can be determined by doubling a low frequency component (using second harmonic generation in a nonlinear crystal) and measuring the difference between it and a high frequency comb mode. For this technique to work the fs comb must have at least an octave frequency span and the number of modes between f_1 and f_2, as well as the mode spacing f_m must be known.

1.3 This Work's Contribution

In the last several years the femtosecond comb method has emerged as the primary way to generate a multiplicity of evenly spaced optical frequency markers that can be tied to a primary atomic standard in a fairly straightforward way. This method addresses the drawbacks of the previously attempted approaches described in Appendix A. However, despite its many benefits, there are certain aspects of the comb that can still be improved. A single comb is limited in spectral extent, and the power in each mode is quite low.

This thesis work describes an optical frequency divider. It is a system that can provide high-power, stable markers at three convenient frequencies to lock two combs together thereby creating a single ultrawideband comb, as shown in Figure 1-2. In addition to locking two combs together our system would allow f_0 to be determined in a different way. By locking the pump or either of the two subharmonic outputs of

the divider to an optical frequency standard, f_0 is obtained by measuring the beat frequency between the divider outputs and the nearest comb line.

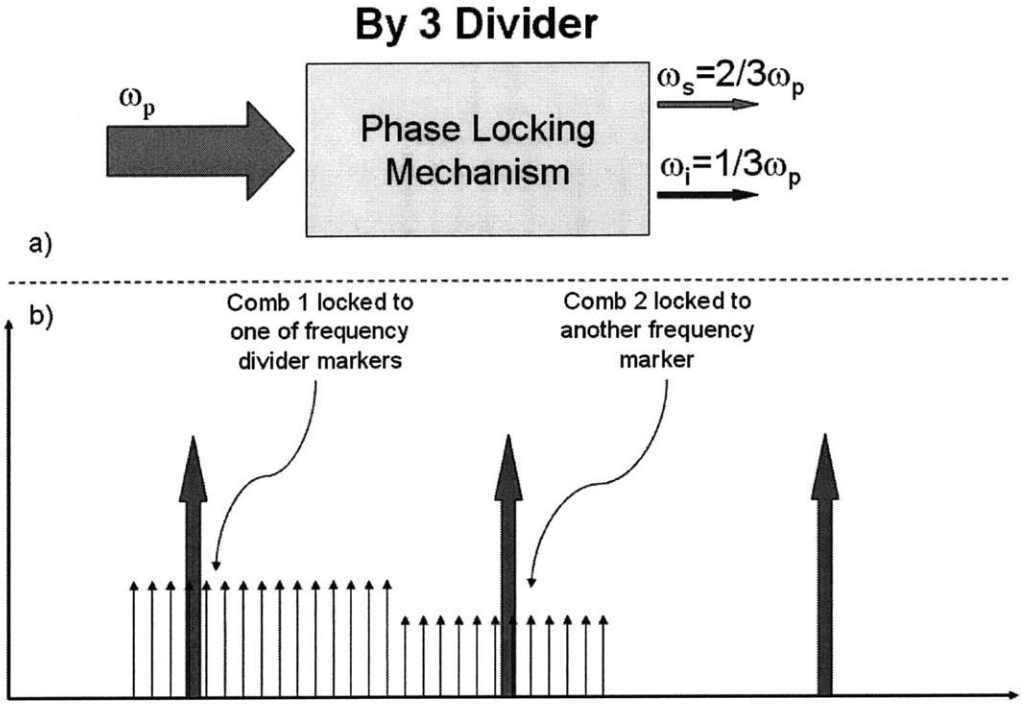

Figure 1-2: A divide-by-3 frequency divider is shown in (a), it is used to lock two femtosecond combs in (b).

This work builds on several other similar experiments. In Ref. [8] a triply resonant optical parametric oscillator (OPO) with a dual section periodically poled lithium niobate (PPLN) crystal pumped by a $\lambda_p = 812$ nm master oscillator power amplifier (MOPA) system and a cascaded second harmonic generator (SHG) allowed self-phase locking to be observed and 3-to-1 frequency division realized. However, the locking range was prohibitively narrow and the pump power of 340 mW was insufficient for stable operation. Another experiment [9] also utilized a two stage PPLN crystal pumped by a 500 mW 532 nm laser to perform 3:1 division. However, in that experiment the two cascaded stages both utilized difference frequency generation (DFG) to produce an RF error signal that was used to adjust the pump wavelength. Furthermore, that experiment required two inputs with roughly a 3:2 frequency relationship.

In the current setup we utilize a dual-grating PPLN crystal with an OPO section

and an SHG section inside a doubly resonant optical cavity to achieve optical self-phase locking. The pump is an 8 W 532 nm frequency doubled YAG laser. Together with a doubly resonant cavity, we expect to obtain a much broader locking range in self-phase locking. We also intend to study the system behavior under high pump power.

Further motivation for this work is derived from the theoretical analysis of the self-phase locked (SPL) OPOs vs. conventional OPOs in [10] and [11]. Several stable solutions are predicted when the self-phase locked OPO is pumped substantially above threshold and close to zero cavity detuning. This behavior, the Hopf bifurcation, is expected to manifest itself as bistabilities within the locking range of the system. This has already been observed in a different 3:1 OPO system for the case where the pump power exceeds the system threshold by a factor of about 4 and with small cavity detuning [12]. However, similar bifurcation is expected for larger detunings at higher pump power, and it has not been observed yet. Observing the rich dynamics predicted to exist in this type of OPO is a goal of the work that will extend beyond the scope of this thesis.

1.4 Thesis Problem Statement

The primary objective of this thesis is to describe the design, construction and operation of a self-phase locked optical frequency divider pumped by a 532.1 nm laser with a signal output at 798.15 nm and an idler output at 1596.3 nm. Although the ultimate goal of this frequency divider is to facilitate the locking of several frequency combs with each other and with a primary standard in order to implement an optical measurement chain spanning from the UV to the IR range of the spectrum, within the context of this thesis the frequency divider is analyzed as a stand alone device.

Chapter 2

Optics Theory

2.1 Introduction

This chapter describes the relevant aspects of linear and nonlinear optics theory that are necessary to understand the behavior of an OPO[1] and SHG. A simple model is introduced to describe the origin of the nonlinear effects. The full mathematical model is described as well; however, no attempt is made to obtain solutions from it. Instead it is noted that the full model can be reduced to a simpler form for the case of large mean fields. The equations for both conventional and self-phase locked OPOs are shown. Criteria that control the efficiency of conversion and the underlying physical phenomena are outlined.

2.2 Nonlinear Interaction

The simplest model of interaction between light and matter is the Drude Lorentz approximation. It models the electrons in a medium as independent masses on springs with a constant spring coefficient. The key phenomenon is that the atoms respond

[1]The same theory and equations describe the behavior of difference frequency generation which is discussed in the experimental section as a means to verify the proper behavior of the crystal.

linearly in phase with the driving field. We can express this mathematically as:

$$P = \chi^{(1)}\epsilon_0 E \tag{2.1}$$

Where P is the polarization density, $\chi^{(1)}$ is the linear susceptibility, ϵ_0 is the vacuum dielectric permittivity, and E is the applied electric field. This model treats the system as a harmonic oscillator. The solutions are well known; however, they are only valid as long as the linearity approximation holds. A more accurate description of the relationship between the induced polarization density and the electric field must include a nonlinear response and can be written as:

$$P = \chi^{(1)}\epsilon_0 E + \chi^{(2)}\epsilon_0 E^2 + \chi^{(3)}\epsilon_0 E^3 + \cdots \tag{2.2}$$

Here it becomes clear that for high electric field amplitudes the polarization is no longer proportional to the field but rather to the higher powers of the electric field. Nonetheless, some insight can be obtained by introducing a term proportional to the displacement squared into the "mass-on-spring" model. When the equation of motion is solved it becomes clear that the solution contains terms at 2ω [13]. The description of the system is further complicated by the fact that Equation (2.2) should be a vector equation where χ is a tensor[2]. Thus a typical element in the full specification of the second order problem may have the form $\chi^{(2)}_{ijk}E_jE_k$. Here we see one of the crucial and fundamental points of nonlinear optics: *the polarization is proportional to the product of several fields; these fields are not required to be at the same frequency.* The implication of this statement is that the output will not be a simple superposition of the input fields as would be expected for a linear system, but rather new frequencies are generated in agreement with the "mass-on-spring" model.

Since in the model $\chi^{(2)}$ has 18 terms[3], the full set of equations describing the

[2]For the most general case where the crystal is anisotropic and dispersive χ is a complex tensor and is frequency dependent, however we will soon see that this large tensor problem reduces to a simple form.

[3]It is a 3x6 matrix where the 3 rows correspond to the 3 components of the induced polarization, and the 6 columns correspond to the permutations of spatial coordinates of the applied field E_jE_k eg. E_1E_1, E_1E_2, E_2E_3, etc.

dynamics of the system may be difficult to solve. Fortunately in real engineering situations the problem can be significantly simplified by reducing χ_{ijk} to a scalar by specifying the polarizations of all the fields to be along the principal axes of the nonlinear medium such as a crystal. In this case the susceptibility $\chi^{(2)}_{ijk}$ is replaced with an effective scalar nonlinear coefficient d_{eff}.

2.3 Phase Matching

A wave propagating through a medium with wavelength λ_n (where the subscript n is the index of refraction of the medium) will have the wavevector $k_n \equiv \frac{2\pi}{\lambda_n}$. In a dispersive medium, the refractive index n is a function of wavelength $n(\lambda)$, and hence fields of different wavelengths do not have the same phase velocities $v_p = \frac{\omega}{k_n} = \frac{\omega\lambda}{2\pi n(\lambda)}$, where λ refers to the vacuum wavelength.

For any nonlinear interaction in a crystal, energy conservation has to be satisfied at the photon level. For the case of the OPO, and any other three-wave mixing process, the energy conservation condition can be expressed as

$$\omega_p = \omega_s + \omega_i, \tag{2.3}$$

where ω_p is the higher frequency pump field and ω_s and ω_i are the subharmonic frequencies of the two output fields. Thus for an OPO, the signal (ω_s) and the idler (ω_i) frequencies must sum to the pump frequency (ω_p). That is, the summed energy of the generated photons must equal the energy of the pump photon. Furthermore, if the phase mismatch between the three waves, defined as:

$$\Delta k = k_p - k_s - k_i \tag{2.4}$$

is not zero, then no specific process is preferred, and therefore several low-efficiency competing processes may occur simultaneously. For example, the power will flow from the pump field to the signal and idler fields as the wave is propagating through the medium and the phase difference Δk is increasing from 0 to π, but then it will

flow back to the pump field as the phase difference continues to increase to 2π. The characteristic length, defined as the distance over which the phase mismatch reaches π, or $l_c = \pi / |\Delta k|$, is called the coherence length, and is the effective length of the nonlinear interaction. The net result of $\Delta k \neq 0$ is that there will be no substantial power in the signal and idler fields regardless of the crystal length.

When the phase matching condition, given in Equation (2.4) and derived from the nonlinear polarization Equation (2.2), is satisfied such that $\Delta k = 0$, only one nonlinear process of interest needs to be considered. As a result we can neglect all other nonlinear processes that are possible under the general tensor χ, but are extremely weak. The phase matching condition (2.4) applies to $\chi^{(2)}$ processes such as the OPO, SHG and difference frequency generation (DFG), all of which are examples of three-wave mixing interactions.

A standard approach to achieve phase matching is to use birefringent materials. In this scenario, waves with different polarizations travel at different speeds; by creating a situation where the three polarizations are not all parallel, it becomes possible to find a temperature or incident angle at which $\Delta k = 0$. The particular set of polarizations and wavelengths depends on the type of crystal and the nonlinear $\chi^{(2)}$ tensor. A more recent and widely used method of achieving high conversion efficiency is via quasi-phase matching; this method is significantly more flexible than birefringent phase matching.

2.3.1 Birefringent Phase Matching

Birefringent phase matching relies on different polarizations having different indices of refraction at the same wavelength. For normal dispersion, the behavior of the ordinary and extraordinary indices as a function of wavelength is shown in Figure 2-1. Phase matching is achieved by the proper choice of wavelengths, polarizations and angles with respect to the crystal's principal axes. The disadvantages of this method are that not all wavelengths can be phase matched, and beam walk-off may become a problem. Since the polarizations are dictated by the phase matching condition it is not possible to freely specify which element of the susceptibility tensor can be used.

In particular, often the largest nonlinear coefficient, such as d_{33} in lithium niobate, cannot be utilized.

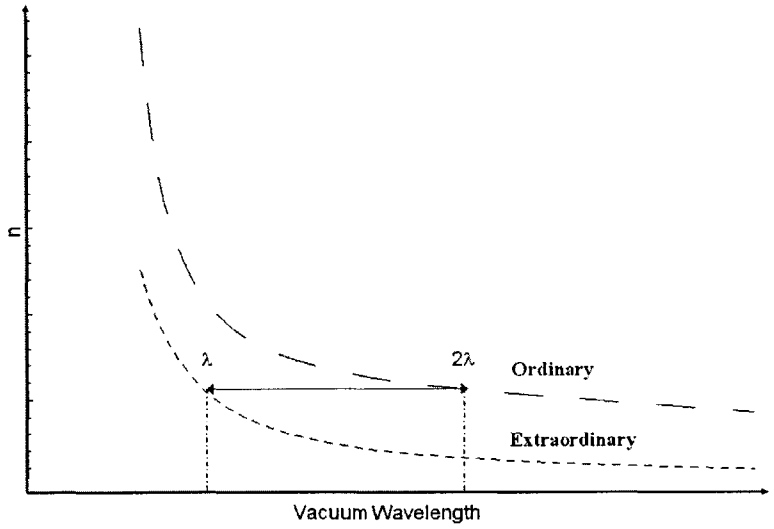

Figure 2-1: Type I birefringent phase matching for second harmonic generation. Ordinary and extraordinary indices of refraction are shown as a function of wavelength.

2.3.2 Quasi-Phase Matching

Quasi-phase matching (QPM) [14, 15] is a technique that allows phase matching of any set of wavelengths over the crystal's transparency range. Instead of being perfectly phase matched, as in the birefringent case, it is possible to offset the effect of dispersion or birefringence and get appreciable field amplitude build-up by periodically resetting the phase lag. This results in a more gradual amplitude increase, but has the benefit of allowing the whole length of the crystal to contribute. This also opens up the possibility of designing crystals that support several simultaneous nonlinear processes in different regions of the crystal. Furthermore, since no limitation is put on the polarizations of the input and outputs, it is possible to chose them such that the largest nonlinear component of χ_{ijk} is utilized. For $LiNbO_3$ with all the fields polarized along the optic axis of the crystal, d_{33} (which is the largest nonlinear component for this crystal) yields an effective nonlinear coefficient $d_{eff} = 2d_{33}/\pi$. This results in an improvement in conversion efficiency by $(d_{eff}/d_{31})^2 \approx 9$ [14] over birefringent phase

matching, which is required to use d_{31}.

QPM is made possible by modulating the susceptibility χ. The phase lag is reset with periodicity l_c such that there is always net power flow from the pump field to the output fields. As explained earlier l_c is the length over which the power flows from the pump to the signal and idler fields. By properly reversing the sign of χ the power flow never reverses direction and hence the output field amplitudes build up over the entire length of the crystal. It becomes clear why this behavior is called quasi-phase matching; the waves do get out of phase locally; however, the phase difference does not increase with propagation over multiple sections of χ reversals.

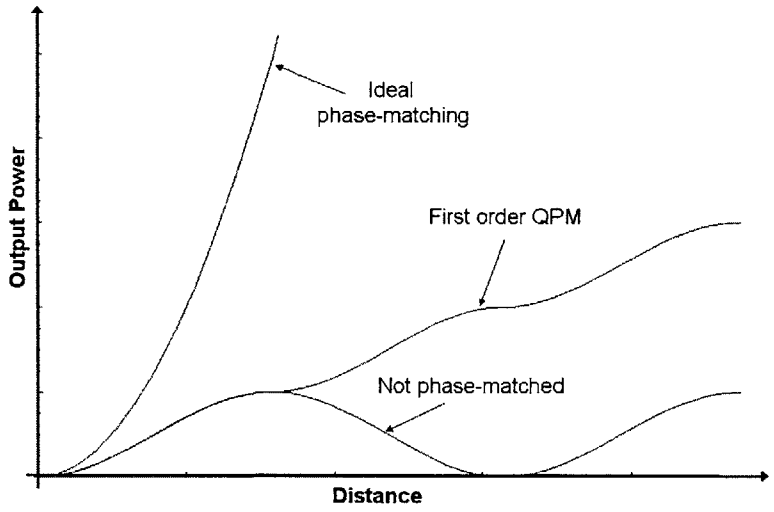

Figure 2-2: A comparison of non-phase matched, first order QPM and ideally phase matched signal power as a function of propagation distance through the crystal.

QPM satisfies the phase matching condition $\Delta k = 0$ by modifying Equation (2.4) to be

$$\Delta k = k_p - k_s - k_i - \frac{2\pi}{\Lambda} \tag{2.5}$$

where $\Lambda = 2l_c$ is the grating period. Since Λ is an artificially applied periodicity, it becomes possible to phase match any set of wavelengths by periodically poling the crystal. Physically the poling is accomplished by periodic reversal of the ferroelectric domains. This is done by depositing electrodes with proper spacing on the crystal and applying a pulsed high voltage to them [16, 17, 18].

An alternative view of QPM involves analyzing the problem in the Fourier domain.

The waves that we are attempting to phase match can be described in terms of their wave vectors k_x, and the mismatch after propagating through distance l is Δkl. The periodic grating structure introduces an additional wave vector which can be shown to be $k_{grating} = \frac{2\pi}{\Lambda}$ [15]. If the poling period is picked appropriately, the phase mismatch will be zero because $\Delta k - k_{grating} = 0$.

2.3.3 QPM Implementation

Equation (2.5) describes the phase mismatch of a periodically poled material with a grating period Λ, and it can be rewritten in a more suggestive form:

$$\Delta k = \frac{2\pi n_p}{\lambda_p} - \frac{2\pi n_s}{\lambda_s} - \frac{2\pi n_i}{\lambda_i} - \frac{2\pi}{\Lambda}. \tag{2.6}$$

Equation (2.6) explicitly shows that the phase mismatch is due to dispersion, and that to calculate the appropriate correction, the indices of refraction of the crystal at each wavelength must be known. Since the polarization in this setup is of Type I, in which all polarizations are along the crystal z-axis, we are interested in calculating the extraordinary coefficient n_e; it is temperature dependent and is given by an experimentally fitted Sellmeier equation [19]. For $LiNbO_3$ the Sellmeier equation is:

$$n_e(T) = \sqrt{a_1 + b_1 \cdot f + \frac{(a_2 + b_2 \cdot f)}{\lambda^2 - (a_3 + b_3 \cdot f)^2} + \frac{(a_4 + b_4 \cdot f)}{(\lambda^2 - a_5^2)} - a_6 \cdot \lambda^2} \tag{2.7}$$

where

$$f \equiv (T - 24.5) \cdot (T + 570.82),$$

T is in °C and the coefficients are given in Table 2.1.

Since the Sellmeier equation and the quasi-phase matching condition give the necessary poling period at the operating temperature, and for fabrication purposes we are interested in specifying the poling period at room temperature, an additional temperature correction must be made to compensate for the expansion of the crystal and thus lengthening of the poling period as normal operating temperatures are reached.

$a_1 = 5.35583$	$b_1 = 4.629 \cdot 10^{-7}$
$a_2 = .100473$	$b_2 = 3.862 \cdot 10^{-8}$
$a_3 = .20692$	$b_3 = -.89 \cdot 10^{-8}$
$a_4 = 100$	$b_4 = 2.657 \cdot 10^{-5}$
$a_5 = 11.34927$	
$a_6 = .015334$	

Table 2.1: Sellmeier coefficients for n_e of $LiNbO_3$.

$\alpha = 1.54 \cdot 10^{-5}$	$\beta = 5.3 \cdot 10^{-9}$

Table 2.2: Thermal expansion coefficients that relate the grating period of the heated crystal to the grating at room temperature.

The temperature correction is given by

$$\Lambda_{corrected} = \frac{\Lambda}{1 + \alpha(T - 25) + \beta(T - 25)^2}$$

and the expansion coefficients are given in Table 2.2.

2.3.4 Temperature Bandwidth

From the Sellmeier equation it is clear that as the temperature is changed the phase mismatch Δk will change, and as a result the amplitude of the generated field will be maximized for $\Delta k = 0$, and decrease as the mismatch becomes larger. The temperature bandwidth of the SHG can be determined from

$$I(\omega_2, z = l) \propto d_{eff}^2 l^2 I^2(\omega_1) \left[\frac{\sin(\Delta k l/2)}{\Delta k l/2}\right]^2 \tag{2.8}$$

where the intensity I is proportional to $|E|^2$, and l is the crystal length. The bandwidth for the remainder of this thesis will be defined as full width at half max (FWHM). Equation (2.8) is obtained by substituting the nonlinear polarization into the the slowly varying envelope equation and integrating over the length of the crystal. It is used to fit the experimental data in Figures 3-4 and 3-5.

2.4 Optical Parametric Oscillator

An optical parametric oscillator is a device consisting of a nonlinear medium in an optical cavity that is pumped by a laser source. This device efficiently converts a high energy pump photon into two lower energy photons. For the case where the energies of the output photons are not degenerate the higher energy output is, by convention, called the signal and the lower energy output is the idler. A schematic representation is shown in Figure 2-3. An OPO, in general, provides any number of pairs of photons at different frequencies as long as they satisfy the energy conservation condition in Equation (2.3).

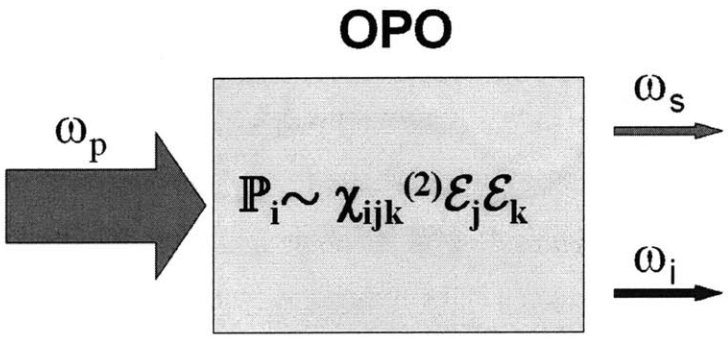

Figure 2-3: A block diagram of an OPO, with the input pump frequency at ω_p and the signal and idler output frequencies at ω_s and ω_i, respectively.

The OPO can be described as similar to a laser. The pump laser provides the gain to the nonlinear medium for the two generated waves. As the down-converted fields travel through the system; they experience losses at the mirrors, the crystal surfaces and the crystal bulk. If the amplification of the signal and the idler per round trip through the optical cavity is greater than the attenuation of those waves then there is net gain in the system, and it is considered to be operating above threshold; the OPO is said to lase. The threshold for an OPO is similar to the condition that must be satisfied for lasing to begin in an ordinary laser. It is determined from a relationship that balances round trip cavity losses with the gain within the crystal.

The initial generation of the fields results from amplification of the vacuum fluctuation that seeds the process. However, upon propagation through the medium and

optical feedback by the cavity, only the photons that satisfy the momentum conservation, or phase matching condition, continue to get amplified. Thus the range of likely output frequencies can be limited by phase matching. A further constraint can be placed on the OPO because only the cavity resonant frequencies build up in amplitude. Just like in a homogeneously broadened laser, only one pair of the signal-idler output goes above threshold and all other resonant mode pairs are suppressed due to insufficient gain. The output frequencies are tunable (depending on the crystal) by adjusting parameters such as, crystal temperature, incident angle, applied electric field and pump wavelength.

A conventional OPO satisfies the energy conservation requirements, and the phase relationship $\phi_p = \phi_s + \phi_i$ which indicates that the sum of the output phases is fixed by the pump phase. However, the phase difference undergoes diffusion and hence ϕ_s and ϕ_i are not determinable [20]. In order for a standard OPO to work as a frequency divider the output phase fluctuation must be stabilized.

One possible way to stabilize the OPO against pair hopping due to fluctuations in the tuning parameters is to phase lock it either by measuring the phase or frequency of the outputs and adjusting the pump wavelength or cavity parameters accordingly; this is called external phase locking. For example an electronic method of locking the phase in a degenerate 2:1 divider relies on a beat note measurement between the output frequencies. The beat frequency is driven to zero by phase locking it to a reference synthesizer [21]. However, this electronic feedback loop has a limited servo bandwidth and introduces noise.

Another way to lock the output phase relationship is by self-phase locking, where intracavity injection locking takes place [22, 12]. This method freezes the phase diffusion with an all-optical process. It can be achieved by adding an extra nonlinearity within the cavity. In the case of 3:1 optical frequency division this enables nonlinear coupling between the two OPO outputs. In practice this means that the crystal has two sections where in the first section the OPO phase matching condition is established, and in the second section the SHG process is phase matched. As the name of this type of OPO implies, the main difference from the conventional OPO is the

phase behavior of the signal and idler waves. The SHG section doubles the idler frequency $\omega_i = \omega_p/3 - \delta$ to $2\omega_i = 2\omega_p/3 - 2\delta$ that is close to the signal frequency at $\omega_s = 2\omega_p/3 + \delta$, and self-injection locking may occur if the frequency difference $\omega_s - 2\omega_i = 3\delta$ is within the locking range. A schematic of the SPL process is shown in Figure 2-4.

The state equations for a conventional OPO in a doubly resonant cavity are taken from References [8] and [23]:

$$\begin{aligned} \dot{A}_p &= -\kappa_p A_p + iDA_s A_i + \sqrt{2\kappa}E_p \\ \dot{A}_s &= -(\kappa_s - i\Delta_s)A_s + iDA_p A_i^* \\ \dot{A}_i &= -(\kappa_i - i\Delta_i)A_i + iDA_p A_s^* \end{aligned} \tag{2.9}$$

where A_x (with x representing the pump, signal or idler) is the complex cavity field amplitude, κ_x is the round trip cavity loss, Δ_x is the detuning of the particular wave from the nearest cavity resonance and D is the nonlinear coupling between the signal and the idler. D is a function of the effective nonlinear coefficient and the length of the OPO section. For a doubly resonant SPL OPO with an additional second order nonlinearity, as is the case in our experiment, the contribution due to the second harmonic section is

$$\begin{aligned} \dot{A}_{s'} &= -(\kappa_{s'} - i\Delta_{s'})A_{s'} + iGA_i A_i \\ \dot{A}_i &= -(\kappa_i - i\Delta_i)A_i + iGA_{s'} A_i^* \end{aligned} \tag{2.10}$$

where $A_{s'}$ is the second harmonic of the idler field shown as $2\omega - 2\delta$ in Figure 2-4. G is the nonlinear coupling strength for the SHG and is a function of d_{eff} and the SHG section length. Generally speaking, the steady state equations are the ones that need to be solved, so the time derivatives are set to zero. Also it is assumed that the pump for each process (E_p for the OPO and A_i for the SHG) is not depleted. The solutions show that unlike a conventional OPO where the phase diffusion is not bounded, an SPL OPO set up to do division by 3 has only 3 acceptable phase states, which means

that exact frequency division can take place [11].

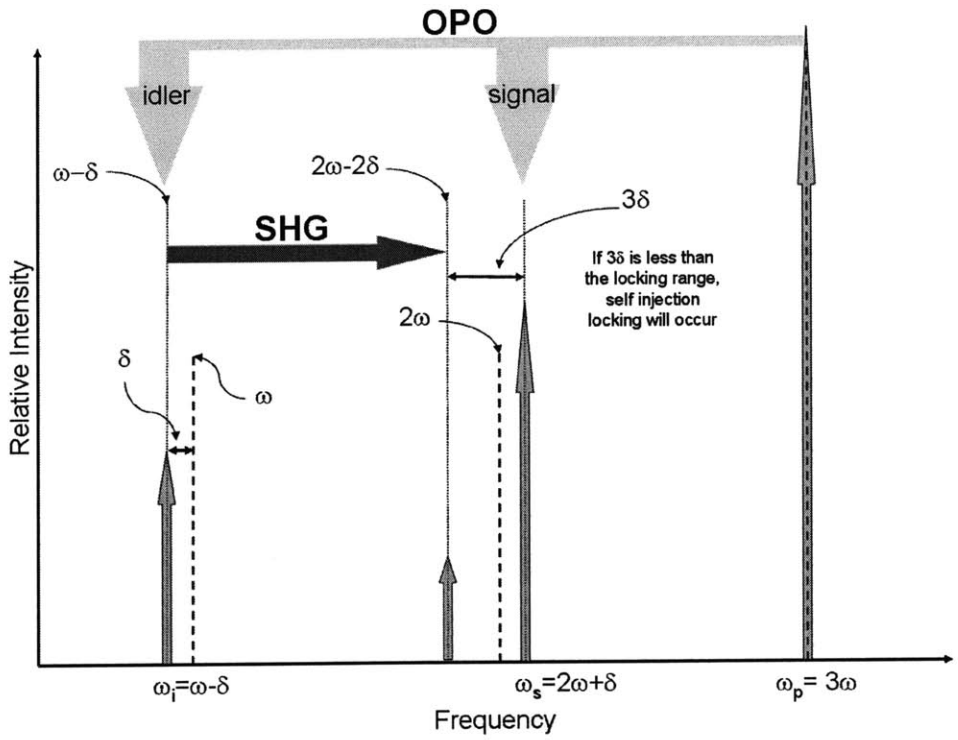

Figure 2-4: A self-phase locked frequency divider utilizing the second harmonic of the idler to injection lock the signal. The pump field at 3ω is the input to the OPO which produces signal and idler outputs at $2\omega + \delta$ and $\omega - \delta$. If the signal and the second harmonic of the idler are within the locking range of the system, the second harmonic of the idler at $2\omega - 2\delta$ injection locks the signal. In this regime $\delta \rightarrow 0$ and exact frequency division by 3 occurs.

2.4.1 Injection Locking

As noted in Figure 2-4, it is possible to build a frequency divider as described in the previous section by utilizing an SPL OPO with the appropriate optical locking. However, for the locking to occur the signal and idler outputs of the conventional OPO component of the 3ω-pumped system must be close enough to the desired frequencies 2ω and ω, respectively. More specifically, they must be within the locking range of the particular OPO cavity configuration.

Injection locking is the mechanism utilized in the SPL OPO and is commonly seen

in laser systems, and can be observed in many coupled oscillator systems in general[4]. Often a spectrally pure but low power master laser is used to lock a free running and more powerful oscillator. Injection locking relies on the limited gain of the lasing medium and suppression of the free running oscillation. When a weak signal at ω_1 is injected into a free running laser oscillator producing intensity I_0 at ω_0, the weak signal can continue to exist simultaneously with the free running oscillation. Since the gain of the medium is much broader than the free running oscillation frequency, the injected frequency becomes amplified if it is within the gain profile of the medium. As the injected signal is tuned closer to ω_0 it is amplified until it begins to rob substantial gain from the free running oscillation. When this happens the oscillation at ω_0 is suppressed and the injected signal is amplified to intensity $\approx I_0$. The range of frequencies around ω_0 within which this suppression of the existing oscillation and amplification of the injected oscillation takes place is called the locking range [24].

This mechanism is responsible for forcing the OPO system to produce frequencies exactly in the ratio of 3:2:1. As seen in Figure 2-4, the SHG doubles the idler produced by the OPO which then injection locks the signal. Since the idler and signal are coupled, as seen from the energy conservation Equation (2.3) and from the OPO Equations (2.9), this leads to the output frequencies moving to exactly 2ω and ω. In other words, $\delta \rightarrow 0$.

An example of what this means can be seen in Figure 2-5, which shows the experimental results of Ref. [12] confirming the theoretical predictions. Figure 2-5 plots the intensities of a non-scanning Fabry-Perot cavity, the pump, and the signal as the OPO cavity length is swept. As the cavity length is scanned it would normally show sharp resonances at the pump and the outputs. However, when the system is operating as a self-phase locked frequency divider the injection locking allows the outputs to remain constant over a much broader cavity length span. Only when the cavity is scanned beyond the locking range of the system does the output disappear.

[4]One of the first observations of injection locking was in 1865 when Christiaan Huygens noticed that two pendulum clocks hanging nearby on the wall would synchronize, but would come out of synchronism if they were spaced out further. The wall provided a coupling mechanism for the mechanical vibrations that coupled the oscillators [24].

2.4.2 Additional Considerations

There are several other effects that can be expected to be seen in an SPL OPO that were not described in this chapter. These include: bistabilities of the subharmonic waves due to competing nonlinearities [10, 11, 12], cascading effects due to the interaction of the frequency doubled idler at $2\omega - 2\delta$ with the pump at 3ω resulting in a field at $\omega + 2\delta$ [12, 25]. Since the SHG process is essentially the same as the OPO, it is possible (under proper phase matching conditions) for the signal $\omega_s = 2\omega + \delta$ to act as a pump for a secondary OPO formed by the SHG section and produce secondary outputs at $\omega + \delta/2 \pm \Delta$. Other details include tuning characteristics and the associated axial and cluster mode hops [26] and reduced locking range with additional pump enhancement [10].

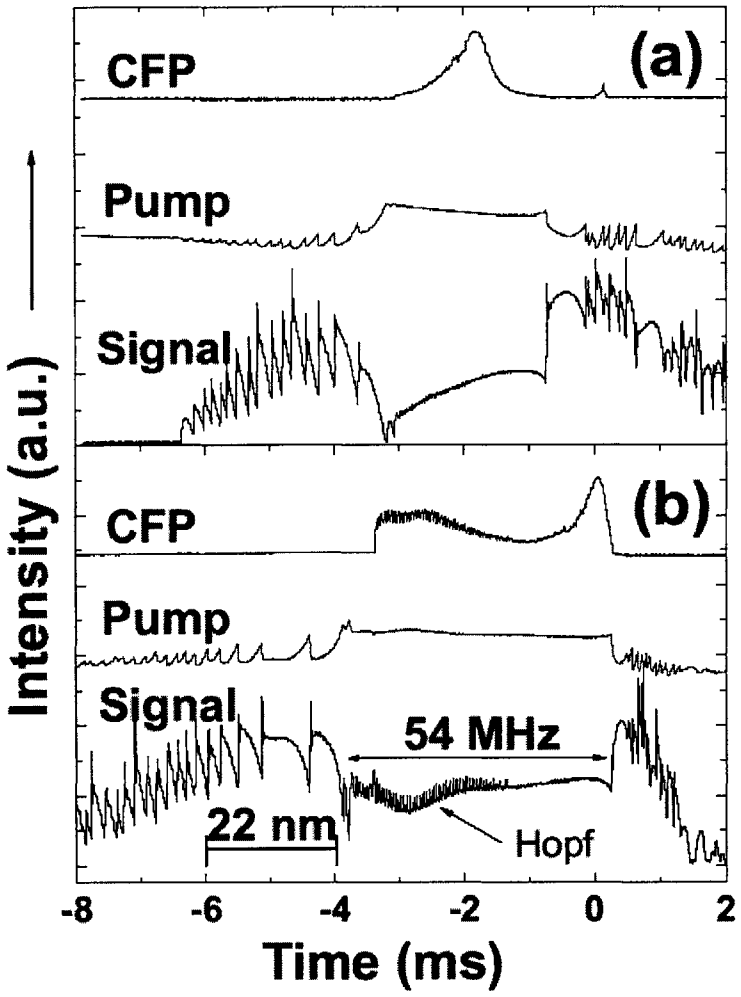

Figure 2-5: Results from a similar experiment performed by our collaborators at BNM, Paris. The data shown is obtained by scanning the cavity length via a PZT. Part **a** shows, in order from top to bottom, transmission from the non-scanning Fabry-Perot cavity, depletion and clamping of the pump power, mode broadening of the signal with non-zero cavity detuning as evidenced by the curved shape of the intensity dip (the idler behavior is qualitatively identical). Part **b** shows the same traces however the cavity is much closer to being on resonance as evidenced by the flatter signal dip. The Hopf bi-stability and oscillation are seen [12].

Chapter 3

Experimental Design and Results

3.1 Introduction

Building a frequency divider is the main purpose of this thesis. The performance metrics of a divider are the conversion efficiency and stability. High conversion efficiency is characterized by a low OPO oscillation threshold, and therefore high output power. The stability of the system can be defined in several different ways. For instance, it is expected that the system will be very sensitive to mechanical vibrations because it relies on crucial alignment of a high finesse cavity for two wavelengths that are nonlinearly coupled to each other within the crystal. Furthermore, it is expected that the system will exhibit sensitive temperature tuning behavior because of the dependence of the indices of refraction on temperature. The main stability metric, however, is the locking range of the system.

Experiments similar to the one described in this thesis have been performed before [8, 9, 12]; however, the full range of theoretical behavior of the system has not been experimentally explored. In addition, previous attempts to perform integer frequency division were severely limited in the amount of pump power available, making observation of Hopf bistabilities unfeasible. Also, previous experiments utilized constant grating period crystals that made smooth phase matching adjustments impossible. The work in Ref. [8], though self-phase locked, exhibited a very small locking range. The work in Ref. [9] was a successful by-3 frequency divider; however, it was not

an OPO, but a single-pass setup with two DFG sections. It was obviously not optically self-phase locked and required an external beat measurement. Furthermore, the single-pass setup required two inputs with roughly 3:2 frequency relationship in order to maintain the exact 3:2:1 ratio. The work in Ref. [12] was a successful triply resonant SPL OPO divider that detected Hopf bistabilities, but only at near-zero cavity detuning because the pump power from the $\lambda \approx 845$ nm tunable MOPA system was limited to only 400 mW, or 4x the OPO threshold.

The motivation for the current work is to address some or all of the above limitations. The generation threshold is kept low by utilizing a doubly resonant cavity; we hope that the stability of the system will be improved by maximizing the locking range and by utilizing custom designed and built semi-monolithic cavity mechanics. This chapter discusses the details of the experimental design as well as the experimental setup and the calculations and trade-offs made in order to obtain the most efficient conversion. The stability of the system is partly controlled by the mechanical and thermal specifications and will also be discussed. It should be mentioned, however, that the efficiency driven decision to employ a doubly resonant cavity instead of a singly resonant cavity also carries certain ramifications for the system stability in terms of its locking range [10].

3.2 Crystal Design, Fabrication and Evaluation

The crystal used in this experiment is a $20 \times 10 \times 0.5$ mm (along the $\hat{X}$-$\hat{Y}$-$\hat{Z}$ crystallographic axis) PPLN. It consists of two sections with different grating periods. The first section is a 13 mm long OPO section; the second section is a 7 mm long SHG section with a fan-out grating. The ratio of lengths was picked based on analysis in Ref. [12] and results from Ref. [9]. A schematic of the crystal with two differently-poled sections is shown in Figure 3-1. By translating the crystal along the y-axis inside the optical cavity it is possible to make the peaks of the two phase matching curves for the OPO and the SHG overlap exactly at the same operating temperature.

We chose PPLN for this experiment because it has the highest nonlinear coefficient

of the commonly used nonlinear materials. The $d_{eff} \equiv 2d_{33}/\pi$ for this crystal is estimated to be $\approx$ 19 pm/V with experimental measurements showing as high as $\sim$ 17 pm/V [27]. PPLN is also highly transparent from approximately 0.35 μm to 5 μm, and by utilizing QPM any three-wave interaction can be achieved. One of the drawbacks of utilizing PPLN is that it has a lower damage threshold than other crystals. The photorefractive damage threshold for PPLN is 10kW/cm^2 at 488 nm, for MgO doped lithium niobate it is 1,700 kW/cm^2 [29]. For comparison a different nonlinear material, KTP, has the damage threshold of 1,000 kW/cm^2.

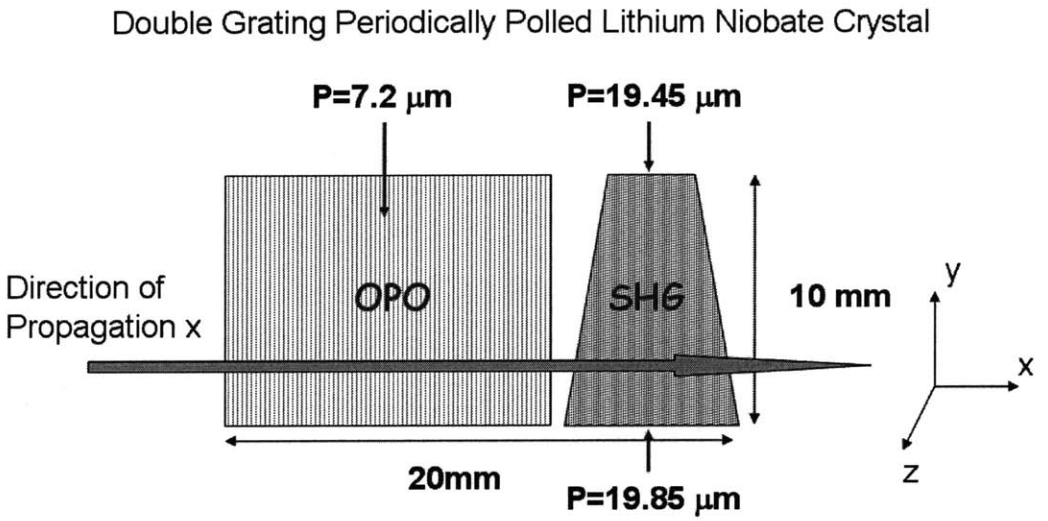

Figure 3-1: Schematic diagram of the double grating PPLN crystal showing fan-out on the SHG section to allow for continuously-tunable phase matching. The x-axis is the direction of beam propagation, the z-axis is the optic axis, and all the fields are polarized along z to use the large d_{33} nonlinear coefficient.

3.2.1 Second Harmonic Fan-Out Grating

For this design we chose to employ a SHG section that has a non-constant grating period. When a dual grating crystal is designed, it is necessary to make sure that the phase matching conditions overlap. Ideally both sections, corresponding to two different nonlinear processes, would be phase matched at the same temperature. However, it is sometimes difficult to accurately predict what poling period will result in proper phase matching due to uncertainties in the empirically obtained Sellmeier equation.

Also, the fabrication process has uncertainties of 0.05 μm for the grating period. The exact effect of this is usually not taken into account when phase matching a crystal.

In order to address the problem of obtaining simultaneous phase matching for two processes in the same crystal it has become common to employ several tracks with slightly different poling periods. By translating the crystal from one track to the next results in a different phase matching wavelength set with a bandwidth that overlaps the adjacent ones. This method gives some flexibility in the design; however, it makes it impossible to continuously tune the overlap of the two phase matching curves. Therefore obtaining perfect overlap may not be feasible, which is undesirable especially when the pump wavelength is fixed as in our case. Despite these drawbacks this method has had some success in the past due to the wide second harmonic bandwidth. Figure 3-2 shows the layout of such a multi-track crystal, and Figure 3-3 shows the bandwidth mismatch that is likely to result with this design.

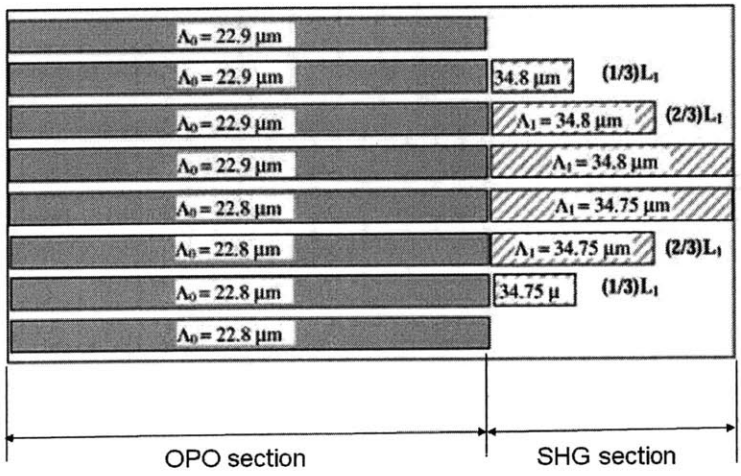

Figure 3-2: A crystal used by our collaborators in France utilizing several tracks with different poling periods to achieve coarse tuning of the bandwidth curves. Furthermore, different ratios of OPO and SHG lengths were utilized to investigate the effect of competing nonlinearities and to experimentally determine the ratio for optimal efficiency.

The method employed in the current work utilizes a crystal with a continuously varying SHG grating period as depicted in Figure 3-1. The clear advantage of this method is that it is possible to continuously tune the crystal by translating it in the beam path. Based on Equation (2.6), the OPO poling period Λ_1=7.2 μm satisfies

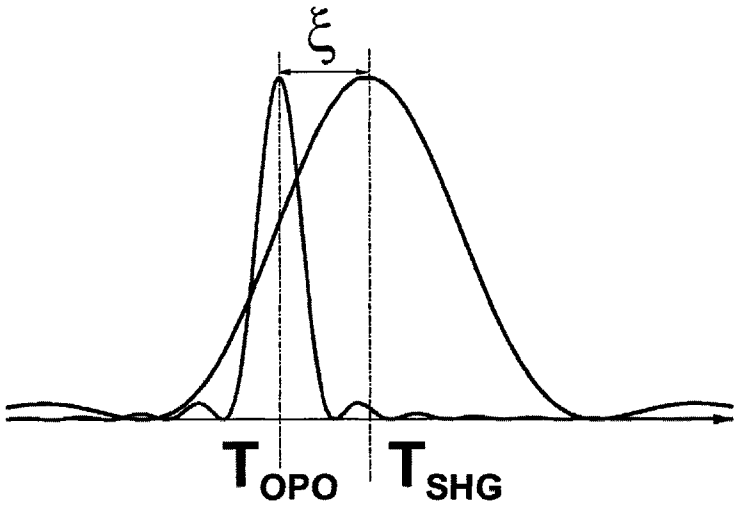

Figure 3-3: Temperature bandwidth mismatch between the OPO and the SHG. This is typical for a crystal with multiple tracks. ξ is the mismatch parameter.

the quasi-phase matching condition at an estimated temperature of 170°C with an expected temperature bandwidth of 1.5°C. The SHG grating period varies along the crystal y-axis from Λ_2=19.45 μm to 19.85 μm. By adjusting the position where the beam crosses the SHG section we are able to effectively change the grating period "seen" by the beam in that section because of our fan-out design. This enables us to overlap the two bandwidth curves exactly as seen in Figures 3-4 and 3-5. This is a significant advantage over the multi-track methods. The disadvantage of this method, at least in theory, is that if the grating period changes substantially over the beam size, the efficiency will be reduced. In order to address this point we were careful to design the fan-out grating such that we had enough tunable range in order to compensate for fabrication or modeling errors in the OPO section while maintaining the grating angle shallow enough so that for our beam size the grating period does not change substantially from one "edge" of the beam to the other. We aimed to achieve 170°C phase matching temperature in the middle of the crystal (i.e. with the SHG poling period of 19.65 μm). The 0.2 μm poling period change to either side of center is substantially greater than the manufacturing errors, and is equivalent to phase matching temperature change of $\approx$ 40°C between the center of the SHG section and one of the crystal edges. For a beam waist of 50 μm the phase matching

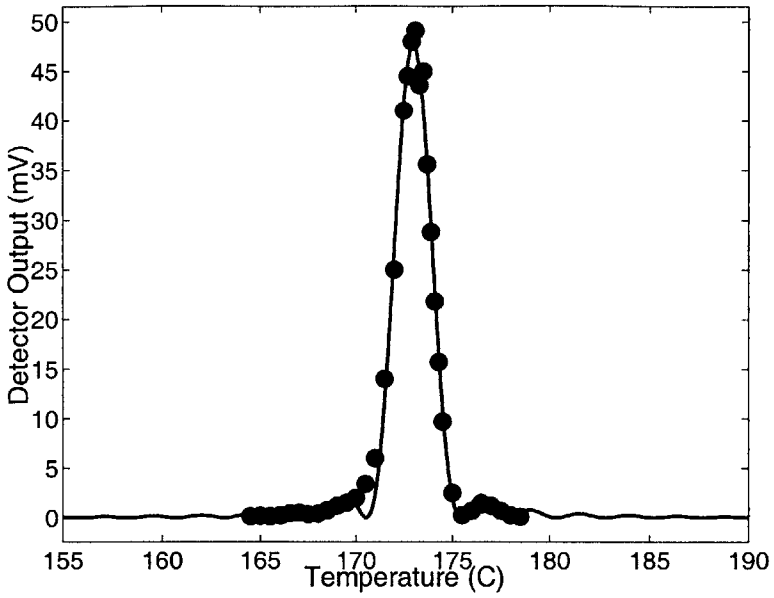

Figure 3-4: Experimental DFG temperature bandwidth and corresponding fitted curve. The inputs used to test the interaction were 532.1 nm and 1596.3 nm beams.

temperature change over the size of the beam is less than 1°C. With the expected SHG temperature bandwidth on the order of 10°C we felt that the grating design specified above provides enough flexibility to be able to compensate for fabrication flaws as well as modeling errors, while not affecting the performance of the system.

3.2.2 Poling Period Verification

Prior to performing any cavity work, the crystal fabrication and theoretical design calculations were verified with two single-pass measurements. We received two PPLN crystals from HC-Photonics. One of the crystals had a poling defect which left a 4×2 mm spot in the OPO section unpoled. The badly poled crystal is the one that we received first, so it was used to check the nonlinear coefficient, the accuracy of our poling period calculation, and the anti-reflection coating applied to the faces.

DFG measurement

We verified the poling period Λ_1 of the OPO section by performing a DFG measurement. A 1596.3 nm beam from a fiber-coupled tunable diode laser was overlapped

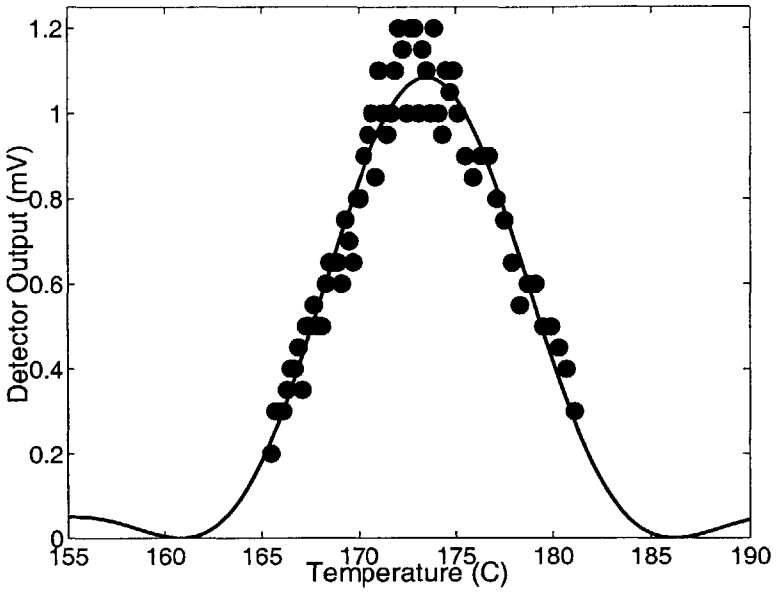

Figure 3-5: Experimental SHG temperature bandwidth and corresponding fitted curve for a fundamental wavelength at 1596.3 nm.

with the 532 nm beam from a Coherent Verdi-8 laser via two apertures spaced by ≈ 2 m; their confocal b parameters were matched inside the crystal. The cw power of the 532 nm beam was varied from 40–80 mW over the course of several measurements. The laser at 1596.3 nm was internally modulated to enable the use of a lock-in amplifier to increase the signal to noise ratio (SNR) of the DFG output at 798.15 nm. The output was reflected off two dichroic mirrors; each one transmitted 90% of the green power and were high reflectors at 800 nm. The output was long-pass filtered with a 700 nm filter, and finally detected with a ThorLabs Si detector. Refer to Figure 3-6 for a simplified schematic of this measurement. To check the uniformity of the poling period the DFG measurement was performed throughout the entire height (y-axis) of the crystal. The output power fluctuation was 20% from one horizontal edge of the crystal to the other. Possible explanations for this include: the poling defect mentioned earlier, coupling between different axes of the translation stage due to misalignment of the crystal or the oven (i.e. as the crystal is moved up it might also be slightly shifted sideways), and nonuniform poling due to fabrication limitations[1].

[1]Due to the process used to periodically pole the crystals, certain diffusion-like effects can be observed. Specifically, as the crystal is translated along the z-axis, the duty cycle of the grating changes slightly.

After accounting for the signal losses in the optics on the output side of the crystal (mostly due to the 10% loss in the long pass filter), and the gain in the detector and filter banks, the average effective nonlinear coefficient from these measurements was calculated to be $\approx$ 8.1 pm/V based on Equation (1) in Ref. [32]. Table 3.1 gives typical parameters and values for the single pass DFG measurements.

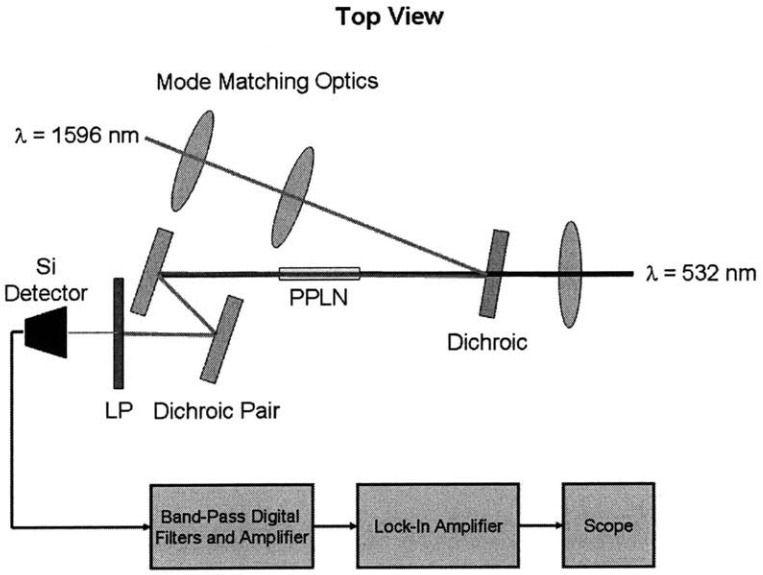

Figure 3-6: Schematic of the DFG measurement.

Interaction	DFG
Input Sources	532.1 nm, 1600 nm (tunable)
Detector	Si ThorLabs PDA55 w/variable gain
Detector Responsivity	.55 A/W
Detector Gain	30 db ($4.7{\cdot}10^5$V/A)
Filter and Lock-In Amp Gain	20 db
Input Power 532 nm (cw)	43 mW
Input Power 1596 nm (10 kHz modulation 50% duty cycle)	760 μW (peak power is twice as high)
Output Voltage	.33V
Calculated d_{eff}	8.1pm/V

Table 3.1: Sample DFG measurement parameters and results

In addition to using the DFG measurement to check the nonlinear coefficient of the crystal, we also verified our phase matching calculations. This was performed by measuring the wavelength and temperature bandwidths and their center points.

The tunable diode laser provided an easy way to change the input wavelength from 1569 nm to 1620 nm and the full-width-half-max (FWHM) wavelength bandwidth was measured to be 2 nm. The temperature of the crystal was swept in increments of 0.1°C and the FWHM temperature bandwidth was determined to be $\approx$ 2.5°C centered at 173.5°C for the 3:1 wavelength. The calculated temperature bandwidth is 1.5°C at 170°C. The temperature bandwidth data along with the fitted sinc^2 curve is shown in Figure 3-4 and in Table 3.3. The wider than expected bandwidth observed in the DFG measurement suggests a shorter effective crystal length of $3l/5 \sim 8$ mm. If this effective crystal length is used, d_{eff} can be recalculated to be $\sim$ 10.4 pm/V.

SHG measurement

In order to verify the accuracy of the Λ_2 calculation and to obtain another measurement of the nonlinear coefficient, a similar single pass measurement was performed in the SHG section. The setup is similar to that in Figure 3-6 with the exception that the 532 nm beam was blocked and the crystal was translated slightly along the x-axis to focus the input beam in the SHG section. The second harmonic of a 2.5 mW 1596.3 nm beam was observed. The laser was internally modulated at 10 kHz and the signal at 798.15 nm was detected by the same adjustable gain Si detector as in the DFG measurement. After the alignment was peaked up the measured signal was .007 V and corresponded to an effective nonlinear coefficient of 9.1 pm/V. The remaining parameters are given in Table 3.2. The temperature of the crystal

Interaction	SHG
Input Source	1600 nm (tunable)
Detector	Si ThorLabs PDA55
Detector Responsivity	.55 A/W
Detector Gain	30 db ($4.7*10^5$V/A)
Filter and Lock-in amp gain	40 db
Input Power 1596 nm (10 kHz modulation 50% duty cycle)	760 μW (peak power is twice as high)
Output Voltage	.007V
Calculated d_{eff}	9.1pm/V

Table 3.2: Sample SHG measurement parameters and results

was scanned in order to measure the temperature bandwidth, and the experimental results are shown in Figure 3-5. The measured bandwidth is $\approx$ 11°C. Figures 3-4 and 3-5 show a perfect overlap of temperature bandwidths at 173.5°C. As described in section 3.2.1, this was accomplished by moving the crystal along the y-axis until the two curves were directly on top of each other. A summary of the calculated and measured temperature bandwidths for both processes is given in Table 3.3.

DFG	Designed	Measured
3-to-1 temperature	170°C	173.5°C
temperature bandwidth	1.5°C	2.5°C
d_{eff}		10.4 pm/V
SHG	Designed	Measured
3-to-1 temperature	162°C	173.5°C
temperature bandwidth	11°C	11°C
d_{eff}		9.1 pm/V

Table 3.3: An overview of the results obtained from the single-pass DFG and SHG measurements and the calculated values.

3.2.3 Crystal Heaters

Two heaters were utilized in the experiment. Initially a heater made by Super Optronics with temperature graduation of 0.1°C and maximum temperature of 220°C was used. This heater was not specifically designed for the crystal size that we employed, so a portion of the crystal extended beyond the internal metal holder which made the temperature in that region unpredictable, and the crystal prone to damage. The crystal, heating element, and temperature sensor were housed in a teflon case. After performing the single pass measurements described above, we received a new heater from the crystal manufacturer specifically designed for this chip size; it also has 0.1°C temperature resolution and stability. The crystal is oriented vertically as shown in Figures 3-1 and 3-10; it is sandwiched between the flat metal heater element and a blank piece of lithium niobate, by two clips. We believed that this method of holding the crystal would enable good thermal contact and allow the entire crystal to thermalize; however, based on the preliminary results it appears that a substantial

temperature gradient exists along the z-axis. The crystal and heater are enclosed in a teflon box with a removable cover.

3.2.4 Crystal and Mirror Coatings

The mirror coatings determine whether the system is a singly resonant oscillator (SRO), doubly resonant (DRO) or triply resonant (TRO). The type of resonator used has a large effect on the threshold power, tuning characteristics and locking range. Based on previous theoretical [10, 11] and experimental [32] work, we chose to implement a DRO with resonances at the signal and the idler wavelengths.

The crystal faces with anti-reflection (AR) coatings are expected to reflect $\leq 0.25\%$ of the incident power at all three wavelengths. The most obvious way to check the losses in the crystal is to determine the attenuation of the laser by measuring the power directly in front of the crystal and directly behind it. However, this method measures a small DC change on top of a large DC bias which results in low SNR due to small power fluctuations of the input beam. Furthermore, this measurement does not isolate a single surface, but rather gives the power attenuation due to reflection at both surfaces as well as losses in the crystal.

A better way to check the coatings is to place a high reflector (HR) in front of the crystal, and then compare the reflected power from an HR mirror with the reflected power from the crystal surface. This assures that the beam parameters at the detector are the same for both measurements. A potential problem with this method is that the detector would be used to compare measurements several orders of magnitude apart which would not yield an accurate result. To overcome this problem several neutral density (ND) filters were calibrated at each of the three wavelengths. They were used to precisely attenuate the signal reflected from the HR mirror in front of the crystal, thus making the magnitudes of the detected signal reflected from the crystal surface and from the HR mirror similar. The schematic of the measurement system is shown in Figure 3-7. The results from the AR coating measurements are summarized in Table 3.4.

The mirror curvatures were selected based on simple cavity stability requirements

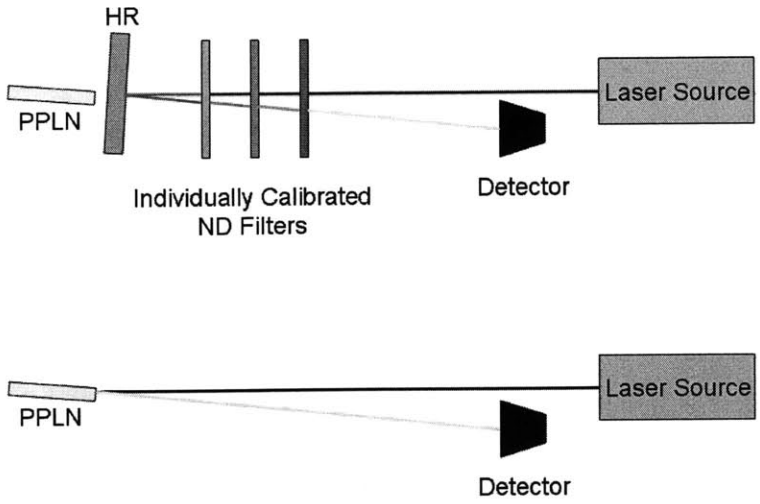

Figure 3-7: The setups used to check the quality of the AR coatings. First, the signal reflected from a HR mirror and attenuated by calibrated ND filters in double-pass configuration is measured. Then the HR mirror and the filters are removed and the signal reflected directly from the crystal face is measured. This method prevents the detector from operating at the different extremes of its range.

Wavelength	1596 nm	798 nm	532 nm
Side 1	0.22%	0.12%	0.25%
Side 2	0.23%	0.22%	0.36%

Table 3.4: Crystal surface reflectivities

such as those shown in Figure 3-11 and the required confocal parameter; cavity size considerations are described in section 3.3.1. We measured the reflectivity of the chosen mirrors by measuring the transmitted power and found it to be 99.95% at 800 nm and 1600 nm. However, when we proceeded to construct the cavity with the custom-made assembly described later in this chapter, we discovered that the mirror curvatures that we chose would require a larger miror separation than we could attain. Therefore we built an asymmetrical cavity with a smaller radius of curvature output mirror. This enabled us to make the cavity shorter. However, the coating of the replacement mirror was not quantified, but we have qualitatively found that it is highly reflecting at the signal and idler wavelengths. Because of this the threshold calculation is slightly inaccurate; however, we do not expect it to be a significant change. As indicated in section 3.5 the mirror coatings not only

determine the threshold power, but the the overall behavior of the system by allowing non-identical losses at the signal and idler wavelengths.

3.2.5 Threshold

Utilizing a doubly resonant oscillator allows the threshold to be dramatically reduced from the ~1 W range expected for an SRO to ~100 mW, which is a very desirable behavior. However, it introduces some difficulties in tuning and implementation. We felt that a low threshold system is crucial to attaining the goals outlined in the introduction of this thesis. Furthermore, a DRO can have a wider locking range than an SRO due to increased coupling strength between the subharmonic waves [10].

Based on Equation (2) from Ref. [32] and from the measurements performed on the coatings of the crystal and the mirrors, the calculated threshold power is 100 mW. In order to determine the threshold experimentally the cavity must first be roughly aligned to allow generation to begin. Pump power on the order of several hundred mW is necessary to achieve the initial oscillation. Once the characteristic resonant clusters at the signal and idler wavelengths are detected during a cavity scan, as seen in Figure 3-8, the mirror, crystal and b parameter are adjusted to improve alignment. This is done by reducing the pump power until the subharmonic waves almost disappear, and then steering the beam, adjusting the crystal position, and changing the beam parameter and mirror positions until the signal is peaked up again. This procedure is repeated until the lowest pump power that still allows the OPO to lase is achieved. The experimentally determined threshold pump power for our system is ~80 mW.

3.3 Optical Resonator

Our optical cavity is a standing wave semi-monolithic doubly resonant cavity design with two concave, highly reflecting mirrors at the signal and idler wavelengths. The cavity is also weakly resonant at the pump wavelength, as shown in Figure 3-8 and 3-9; this helps with initial alignment. The purpose of the cavity is:

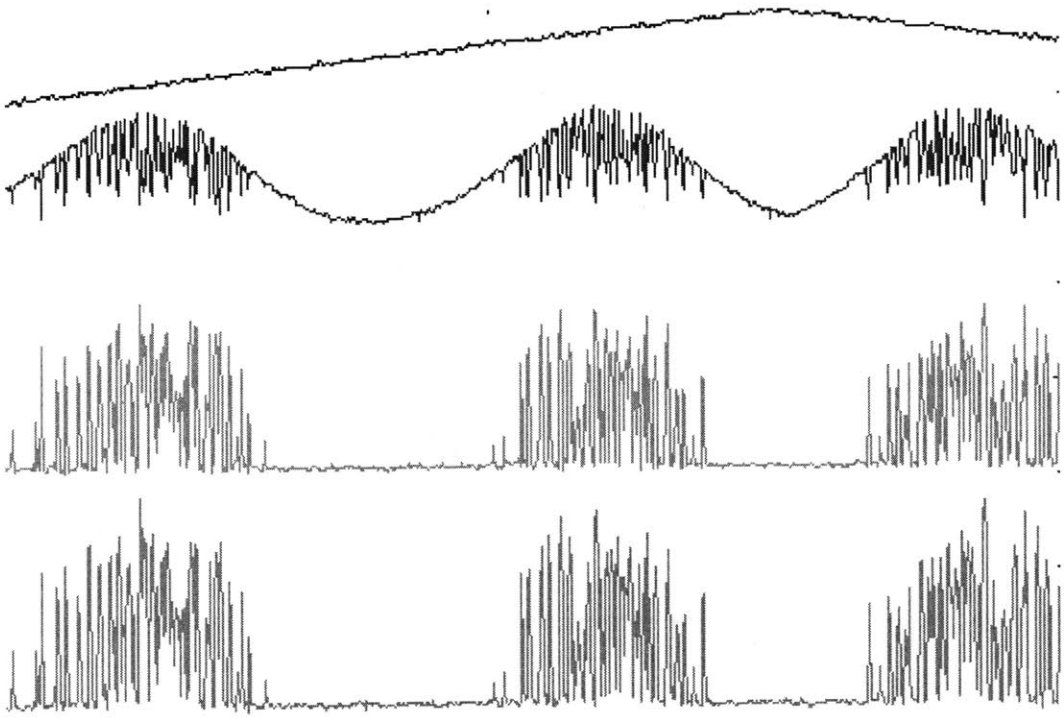

Figure 3-8: Typical cavity scan showing generation of signal and idler waves. The top trace is the cavity PZT scan voltage. The horizontal axis is the time during a scan, the vertical axis is amplitude from the output pump, signal, and idler (top to bottom) detectors. At this time scale the individual fringes cannot be resolved, but the signal and idler behavior are identical. The crystal temperature is 185°C.

- To allow for optical feedback between the OPO and the SHG sections, which enables self-phase locking;
- To amplify the signal and idler waves, thus reducing the threshold power; and
- To slightly amplify the pump power, which aids in cavity alignment and lowers the threshold.

The cavity is non-symmetric, with the input mirror radius of curvature $R = 6.0$ cm and the output mirror $R = 2.5$ cm. Both mirrors are 7.75 mm in diameter, 4.0 mm thick and they are separated by 8.5 cm. Figure 3-10 shows the schematic of the cavity. The input mirror is mounted on a piezo-electric transducer (PZT) consisting of 4 ring-shaped elements appropriately wired up and held together by electrically conducting epoxy. We chose to use four individual elements to make the PZT based on two considerations: first, in order to cover a free spectral range at the longest

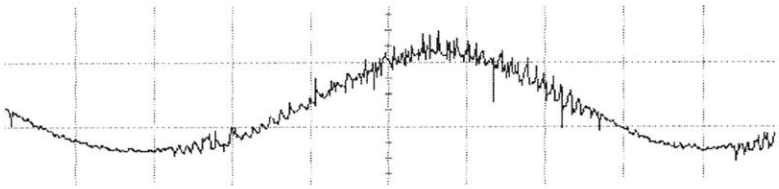

Figure 3-9: Sinusoidal pump power at the output of the cavity during a cavity length scan shows that the cavity is weakly resonant at this wavelength. This was useful during the initial alignment because the pump power was high, and the cavity was not very sensitive to pump misalignments.

wavelength, the cavity length must change by at least half the wavelength (i.e. 800 nm); second, with an even number of elements in the PZT, the outer parts of the outer rings are connected to ground, with the high voltage applied only to the inner components. The second measure is strictly a safety precaution. The expansion coefficient of the PZT rings is $\sim$ 500 pm/V and the highest reasonable voltage that can be applied is $\sim$ 600 V. Thus in order to achieve the necessary scanning range, 3 elements would have been sufficient; the fourth element is in fact a slight drawback because it slows down the response time of the PZT. This will become relevant once the cavity servo is implemented; however, we do not foresee it as a problem.

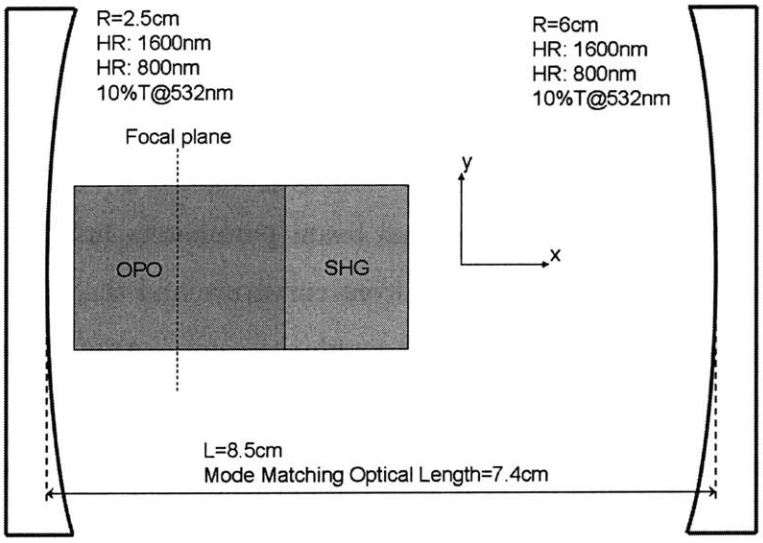

Figure 3-10: The crystal inside the cavity and cavity parameters. The effective mode-matching optical cavity length is shown. The effective length from the b parameter perspective is actually longer than the physical length. Note that the drawing is not to scale.

3.3.1 Optical Design

Since the key criterion that dictates the optical design is efficient conversion within the crystal, the appropriate method to design an optical system is to begin with the crystal itself and assume that the conditions necessary for efficient conversion are met. Then the pump beam is propagated backwards outside of the crystal, through the input cavity mirror, and appropriate optics are placed in order to mode-match with the incoming beam from the laser. Aligning elements such as beam steering optics and means to adjust the beam parameters also need to be provided.

It has been shown with theory [31] and experiment [32] that the conversion is optimized when the b parameter of the pump beam inside the crystal is approximately equal to the length of the crystal, or more precisely the length of the OPO section, with the focus in the middle of the OPO section.

Before beginning to back-propagate the beam out of the crystal it must be noted that the final solution must adhere to two stringent criteria. First, the beam entering and leaving the crystal must be small enough so as to not be clipped by the 0.5 mm thick (along the z-axis) crystal. If the crystal is treated as an aperture that is 500 μm in size, the beam diameters for all three wavelengths at both edges of the crystal should be less than $\approx 160\ \mu m^2$. Second, the cavity that provides the resonance for the idler and the signal and weak resonance for the pump must be stable. The stability condition is quantified and explained in Ref. [30]. Simply put, it means that after a round trip through the cavity the final beam parameters must match the initial ones; more specifically, the beam phase front curvature and the beam waist must be identical before and after a round trip through the cavity. Another way to view this condition is that to establish a standing wave in the cavity, at the mirror surfaces the phase front curvatures must exactly match the mirror curvatures. Usually the stable regions are easily determinable from the mirror curvatures. For instance, in the current setup with the input and output mirrors having the curvature R=6.0 cm and R=2.5 cm, respectively, the cavity is stable for mirror separation between 0 and 2.5

[2]As a rule of thumb, negligible losses will occur if the beam waist is at least 5-6 times smaller than the aperture.

cm and 6.0 and 8.5 cm. To calculate the exact behavior of the beam inside the cavity as the cavity parameters (such as length or mirror curvature) are changed, a complex beam parameter q is introduced. It encompasses both the phase front curvature and the beam radius at every point. The stable solutions for our particular cavity are shown in Figure 3-11.

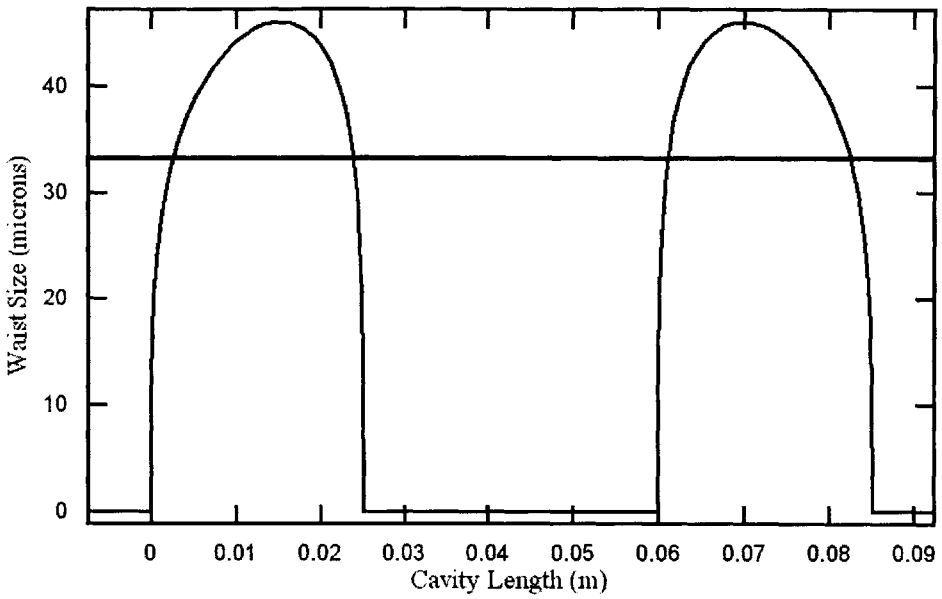

Figure 3-11: Beam waist as a function of cavity mirror separation for the cold cavity with R=2.5 cm and R=6.0 cm used in the experiment at λ = 532 nm. Note the two stable regions corresponding to cavity lengths 0.0–2.5 cm and 6.0–8.5 cm. Due to minimum cavity length constraint of 4 cm determined by the size of the crystal heater assembly we were operating in the second stable region. The horizontal line is at the desired 33 μm waist. Also note that in order to obtain it the cavity has to be far from the most stable point.

The presence of the crystal has two effects on cavity design. First, the b parameter inside the crystal is larger than in free space by a factor of n; this can be verified by considering Snell's law. In other words, a converging beam incident on the surface of a crystal with n>1 will converge less sharply inside the crystal. Thus the focus with the crystal in place will be further; however, the waist size will be the same as if the crystal were absent. Second, the effective cavity length is shorter. This result comes from the effect of n on the phase front curvature. This means that an empty cavity that is too long and on the verge of being unstable may become stable once the

crystal is placed inside. An additional consideration that must be accounted for is that the input mirror to the cavity acts as a lens and modifies the beam parameters.

To have the b parameter of the pump equal the length of the OPO section requires that the waist be 33 μm according to $b = \frac{2\pi w_0^2}{\lambda}$. As seen in Figure 3-11, to achieve this requires that we operate near a cold-cavity length of 8 cm, which is on a steep slope. For stability consideration it is preferred to operate on a more gentle slope near the 7 cm mark in Figure 3-11. Therefore, our cavity is shorter than would be required to have the optimal b for the most efficient conversion. Although the value of the b parameter has an effect on conversion efficiency, the dependence is not very strong. A b parameter twice as long as the OPO section would be only marginally less efficient. As such, the desired b parameter was only a starting point for the cavity alignment. In the experiment the cavity length was adjusted to have the strongest TM_{00} mode with as little power as possible in the higher order modes. As seen in Figure 3-10 the effective optical length, for mode matching purposes, is 7.4 cm, and by using this number in Figure 3-11 we see that this corresponds to approximately 45 μm waist. Not surprisingly, this is near the middle of the stable region.

We adhered to the following steps to design our cavity:

1. Determine the necessary b parameter inside the crystal;

2. Reduce to an analogous problem without the crystal. The focus is closer by d/2n where d is the length of the crystal. The b parameter is shorter by $b_{air}=b_{crystal}/n$. The waist remains the same;

3. Calculate the necessary cavity mirror separation to obtain the desired b_{air};

4. Check that the answer is feasible given the hardware specification; and

5. Transform the b parameter inside the cavity to the b parameter outside the cavity. The difference is due to the input mirror acting as a lens.

3.3.2 Mechanical Design

The criteria on the mechanical design of the cavity are to keep the mirrors in proper angular and linear alignment in order to facilitate proper interaction within the crystal, and to provide an enclosure that helps maintain the crystal temperature constant by reducing convection air currents.

Vibration Tolerance

One of the considerations in this work is the stability of the system. Since it is generally very sensitive to vibration, mechanical stability becomes a crucial factor in the cavity design. Many optical cavities are designed as two or more separate free standing mirrors on mounts attached to the optical table. In order to reduce flexure in the mounts, the mirrors are usually kept very close to the table surface. The free-standing arrangement has the benefit of allowing fine angular adjustment of the mirrors that makes tuning and alignment easier. However, these same mechanics also respond to vibration because every adjustable mirror mount has non-rigid spring-loaded components. The free-standing arrangement also makes it nontrivial to modify the mirror separation while maintaining mirror alignment without resorting to the use of translation stages. Translation stages, however, also have vibration-sensitive spring loaded elements.

An alternative approach is to use a monolithic cavity. Typically it is made from a solid block of aluminum with a hollowed out interior and a drilled hole for the beam path. The mirrors are glued directly to the aluminum faces. Though this arrangement offers superb vibration resistance, with both mirrors attached to the same piece of metal, changing the mirror separation or angles requires re-gluing, thus making fine alignment changes impossible. The only way to properly align an input beam into this sort of cavity is by steering the beam itself.

The cavity used in the current experiment is custom made, and it allows for the mirror separation to be easily modified and for the mirrors to be translated in the plane perpendicular to the beam. Since the mirrors are curved, this translation is

equivalent to performing angular adjustments. Once the cavity is tuned the retaining bolts can be tightened down so that it forms a solid block. The cavity comprises a

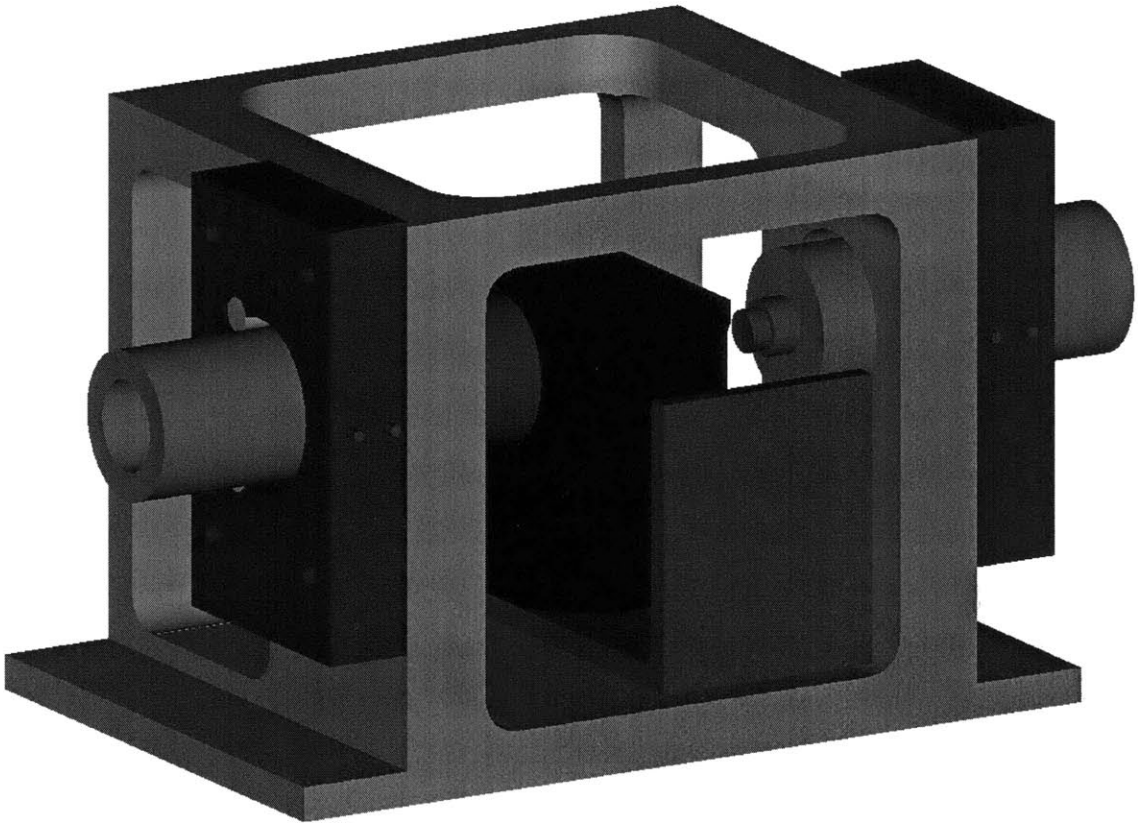

Figure 3-12: Cavity mechanical design.

central piece, two thick end plates that are bolted to it, two mirror mounting tubes that are free to slide through the end plates and the necessary hardware to assemble the structure. Figure 3-12 shows an AutoCad rendering of the full assembly.

The central piece was machined from a solid $4'' \times 4'' \times 6''$ block of 6061 aluminum. Two flanges at the base allow the piece to be clamped down to the optical table. The interior has been hollowed out with the necessary access holes made for the crystal, heater, and the heater enclosure. The heater assembly is mounted on a right angle bracket which is attached to a three axis stage on top of a two axis goniometer. In addition to housing the crystal heater, the central piece provides a mounting platform for the adjustable components. The dimensions of the central piece after machining are given in Table 3.5 and the three-views of the piece are provided in Appendix B.

Outside Length	11.4 cm
Inside Length	8.2 cm
Outside Depth	10 cm
Inside Depth	7.7 cm
Outside Height	10 cm
Inside Height	7.7cm
Maximum y-axis Heater Translation	2.7cm
Maximum z-axis Heater Translation	limited by cavity length

Table 3.5: The dimensions of the central cavity block

Two 3 cm-thick aluminum end plates are attached to the central piece via over-bored holes in the plates, four bolts, and tapped holes in the central piece. This allows the plates to translate by 3 mm vertically and horizontally in the plane perpendicular to the beam. In order to achieve the smooth translation each plate was temporarily epoxied to a 2-axis stage. Once the alignment was finished, the plate retaining bolts were tightened to prevent further motion. Each plate has a large circular hole with two smaller holes along its circumference. Two 3/8" steel pins were pressed into the smaller holes and act as rails to guide the 7.5 cm long mirror mounting cylinders. The third anchor point for the cylinder is provided by two nylon tipped set screws which press the cylinder into place against the steel pins after the appropriate cavity length has been established. The large hole in the plates is $\approx$ 3 mm larger than the 1" mirror mounting cylinder. A closeup of the cylinder and plate assembly is shown in Figure 3-13.

The mirror mounting cylinders were lathed from 7075 aluminum bar stock. Their outside diameter was turned down to be 1" in order to fit loosely into the holes in the side plates and to comply with standard 1" optical mounting hardware. All the aluminum components of the cavity were black anodized to increase the surface hardness and reduce the reflection of scattered laser light.

This system has several benefits. Once it is bolted together, there are no spring loaded components in contact with the mirrors, so the structure behaves as if it were monolithic. Adjustments are possible by changing the mirror separation from $\approx$ 1

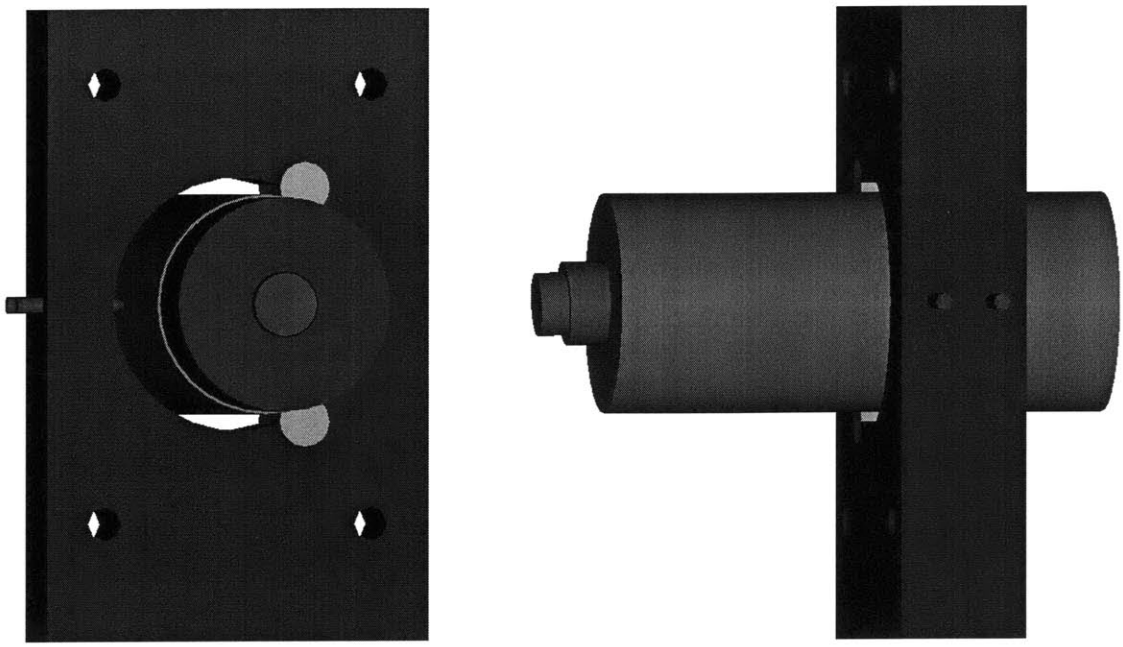

Figure 3-13: Closeup of the mirror mounts. On the left a mirror mounting tube and a standard 1" mount with the curved cavity mirror are shown. The end plate with its two steel pins and set screws is also seen. On the right an identical mirror mounting tube and plate are shown, but instead of a standard mirror mount, a PZT stack is used. The faces of the stack are not parallel to each other as described in the text.

cm to $\approx$ 10 cm, and thereby changing the cavity parameters. The mirror mounting cylinders are free to rotate around their axes, which adds another degree of freedom that has proved to be useful in aligning the cavity. Finally, the side plates are free to move perpendicular to the beam. The mirrors can be mounted on standard 1" circular mounts epoxied to the mirror mounting cylinders of the same diameter. This makes mirror replacement an easy task. Furthermore, if in the future this assembly is used to make another cavity it could easily incorporate 1" mirrors directly inside the side plates or glued to the mounting cylinders. As an example of the stability of the alignment of this semi-monolithic cavity it should be noted that the OPO works without realignment with the same threshold power after an idle period of 2 months.

Thermal Requirements

As shown in Equation (2.7) the temperature dependence of the conversion processes is quite strong. Furthermore, based on results from 2.3.4 and experimentally verified

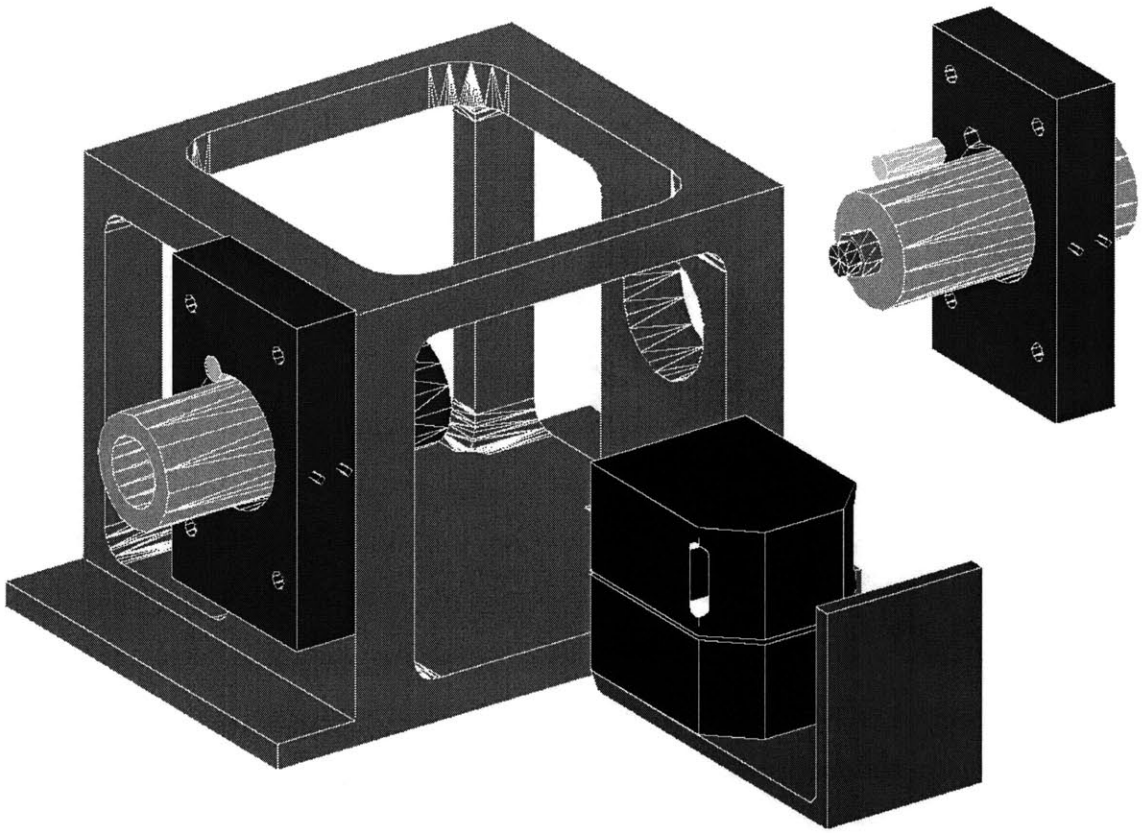

Figure 3-14: Cavity mechanical design, exploded view.

data from 3.2.2 it can be deduced that precise temperature tuning will be a key factor in obtaining the sought-after experimental results. In order to reduce the effects of temperature fluctuation on the experiment, the mechanical design of the cavity allows it to be enclosed to reduce convection currents. Additionally, the cavity and all the immediately associated controls and optics will be enclosed in a plexiglass container to further reduce the effects of temperature swings and acoustic vibrations.

3.3.3 Alignment

Mode-matching into a cavity with a crystal inside requires an approximate determination of the necessary optics and a methodical search through the alignment parameter space. Several "knobs" provide the necessary controls in order to obtain proper alignment and mode-matching. Because the cavity is designed to reduce vibration, it has no angular adjustment for the two mirrors, and the following alignment procedure

was used. The beam was steered via two flat mirrors outside the cavity; the cavity mirrors were translated perpendicular to the beam and their separation was coarsely adjusted; the input beam parameters were adjusted via two lenses mounted on translation stages.

The general procedure that we followed for aligning our cavity was as follows. Since the cavity is weakly resonant at the pump wavelength, after performing the calculations to achieve the correct effective beam waist "looking" into the cavity we removed the input cavity mirror and reflected the pump beam from the output mirror. With the beam hitting the center of the back mirror we overlapped the input and the reflected beam. The input mirror was replaced but put in backwards in its mount, and the beam alignment was double checked. It turned out that in our setup, although the metal mounting structure used for the cavity assured good alignment of the mounting components, the limiting factor was the PZT stack which made it difficult to assure the parallelism of the input and output mirrors. After this rough check on alignment was made, the input mirror was put back in its appropriate configuration. With everything assembled the two mirrors were not perfectly parallel. More precisely, the input mirror, which is mounted on the PZT stack, was not parallel to the face of the mounting cylinder. However we were able to compensate for this error by translating the mirrors perpendicular to the beam and by rotating them around the beam axis.

With pump power of about 50 mW we looked for pump resonances as the cavity length was scanned. Eventually a resonance as seen in Figures 3-8 and 3-9 was detected. One of the problems that we noted was that even while the cavity was at a stable length and aligned for resonance without the crystal, when the crystal was placed inside and the cavity appropriately lengthened, no resonances were seen and the system had to be realigned. We attribute this to non-parallel crystal faces which force the beam inside the cavity to propagate off-cavity-center. Thus little is gained by aligning the cold cavity because as soon as the crystal is placed in the beam path, the cavity parameters would have to be modified and the mirrors realigned. Nonetheless a cavity finesse measurement was performed with the cold cavity to characterize the mirrors and to familiarize ourselves with alignment techniques. The

original intention was to repeat the measurement with the crystal in the cavity in order to use the two finesse measurements to accurately determine the losses in the crystal, and thus obtain a more accurate estimate of the threshold power. However, after the cold cavity finesse was measured, and the crystal was placed inside, we directly proceeded to align the cavity and characterize the OPO behavior. Thus a cavity-with-crystal finesse was not measured.

Finesse Measurement

Based on the previously described mirror coating measurements, the cavity finesse, defined as $F = \pi\sqrt{R}/(1-R)$, is expected to be ~6000 where R is the mirror reflectivity. The finesse is a measure of the "quality" of the resonator, and therefore its frequency selectivity. With the empty cavity we checked the finesse, at 1600 nm, by measuring the ratio of the spacing between two adjacent resonant peaks, separated by one free spectral range (FSR), and the peak width. This measurement was performed by scanning the cavity length at two different rates. First, an 80 Hz, 2 V_{p-p} saw-tooth was amplified by a high voltage amplifier (4 channel variable gain Trek 601B-4) and applied to the PZT.

The spacing between two peaks separated by one FSR detected on an oscilloscope was 4.49 ms. Second, the cavity was scanned at 60 Hz with the amplitude 0.5 V_{p-p}. The bias voltage was adjusted to bring one of the resonant peaks into view; the amplitude was reduced from the previous measurement in order to better resolve it, and its FWHM was 12 μs. One idler FSR is shown in Figure 3-15; a closeup of one of the peaks is shown in Figure 3-16. The scan rates were used to calibrate the time measurements. In the first case the PZT was scanned at 160 V/s; in the second case it was 30 V/s. Thus the finesse is

$$F = \frac{160(V/s)}{30(V/s)}\frac{4.49(ms)}{.012(ms)} = 1995 \tag{3.1}$$

This value is somewhat smaller than the prediction based on the measurement of the mirror coatings; for the particular application, however, the actual finesse is of little

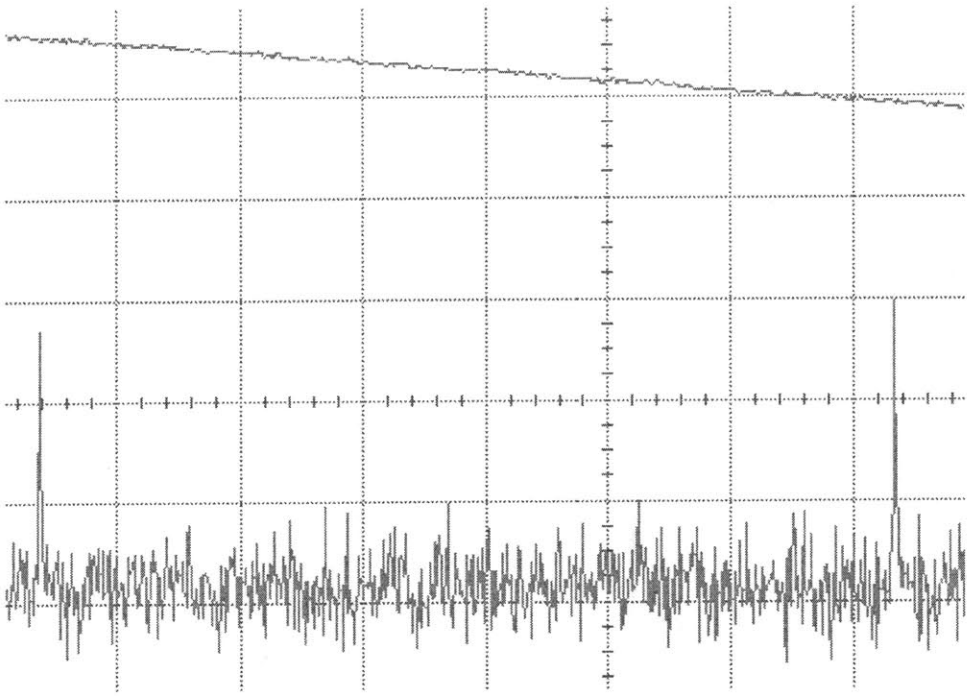

Figure 3-15: The top trace is the PZT voltage ramp. The bottom is one full free spectral range showing cavity resonance at the idler wavelength.

importance as long as the cavity is highly resonant at the signal and idler wavelengths. We have also estimated the finesse of the weak pump resonance, shown in Figure 3-9 to be $\leq$20. Furthermore, it should be noted that the original idler finesse calculation yielding F=6000 was done using the data from two identical mirrors with 6 cm radii of curvature. Since then, one of the mirrors has been replaced with what appears to be a slightly less reflective mirror. Finally the method used to check the mirror coatings is less accurate than the finesse measurement described here. In practice, cavities with finesse exceeding several thousand are not very common.

3.4 Detection Scheme

The detection system consists of beam splitters, attenuators, filters, detectors and a wavemeter, and is shown in Figure 3-17. The output of the OPO is sent to a dichroic which reflects most of the signal power and a small amount of the pump. The transmitted light consists of the idler and the pump. The idler is detected using a 50

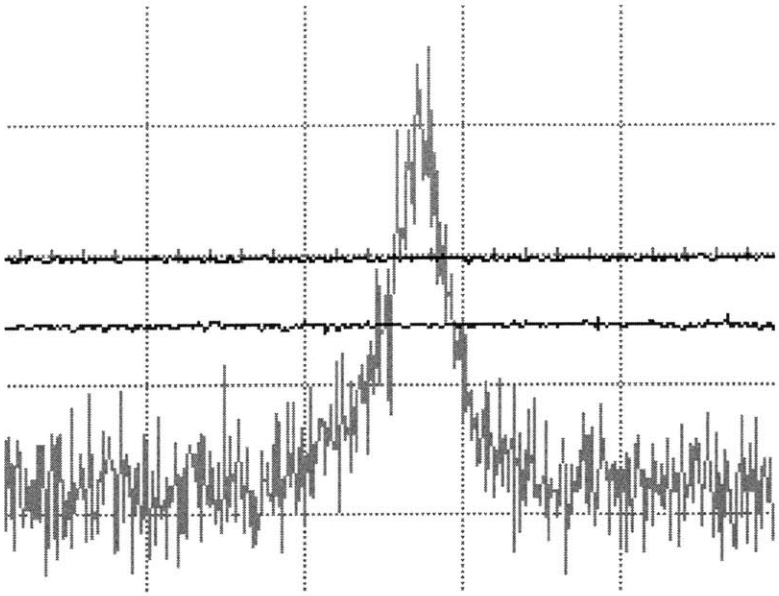

Figure 3-16: A closeup of one of the idler resonant peaks during a cold cavity scan.

MHz bandwidth ThorLabs PDA255 InGaAs amplified photodetector. This detector is very weakly sensitive to the signal wavelength, and not sensitive to the pump wavelength. To cut out the residual signal power a 1 μm long-pass (LP) filter is used. The reflected beam is split into the signal and the pump by the .7 μm cut-off LP filter. The weak pump resonance shown in Figure 3-9 was observed using a "home-made" amplified Si detector using an EG&G FFD100 photo-diode. Because Si photodetectors are sensitive to both the pump (532 nm) and the signal (798 nm), but not to the idler (1596 nm) wavelengths, a 532-nm pass filter was used to select only the pump for detection. For signal detection we using an amplified 10 MHz bandwidth ThorLabs PDA55 photodetector. The beam is split using a non-polarizing 50/50 beam splitter (BS). One beam is used to monitor the real-time behavior of the signal, the other is directed into a Coherent WaveMaster wavelength meter. While studying the behavior of the system, the cavity length was scanned as various parameters were tuned; however, periodically the PZT scan was disabled and the wavelength meter allowed us to determine if we were near the correct divide-by-3 regime.

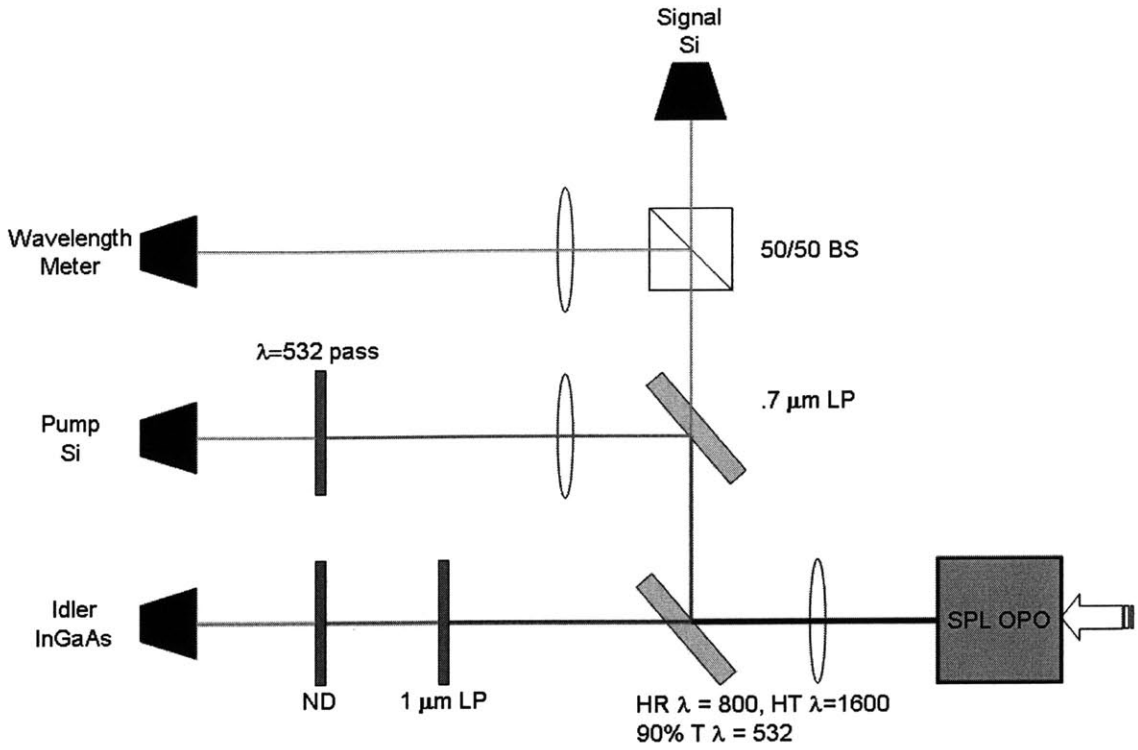

Figure 3-17: The detector setup used to monitor the pump, signal and idler simultaneously, as well as measuring the signal wavelength to verify the divide-by-3 behavior. In the future the detector system may include a Fabry-Perot etalon to distinguish the 3 allowed phase states, as well as an additional crystal to double the idler and measure the beat with the signal to obtain further verification that the divider is working in the proper regime.

3.5 Preliminary Results

In studying the behavior of our system and attempting to find the exact divide-by-3 point we have made several observations. Some of these agree with previous works on self-phase locked OPOs and integer frequency divider experiments; whereas other observations we cannot yet fully explain. Our system was designed to be phase matched for proper operation at 170°C; we have used single pass measurements to verify this behavior and have found that both the OPO and the SHG operate as expected at 173.5°C with the crystal in the Super Optronics oven. After the AR coatings on the crystal and the HR coatings on the mirrors have been checked and the cold cavity idler finesse measured, we proceeded to align the cavity with the crystal inside the HC-Photonics oven and search for the expected subharmonic wave

generation and eventual self-phase locking. We have observed the OPO operating above threshold over a broad range of temperatures from $\sim$ 155°C to $\sim$ 210°C as shown in Figures 3-8, 3-18, 3-19, and 3-20, which show the cavity length scan, and the pump, signal and idler traces (from top to bottom, respectively). After the initial

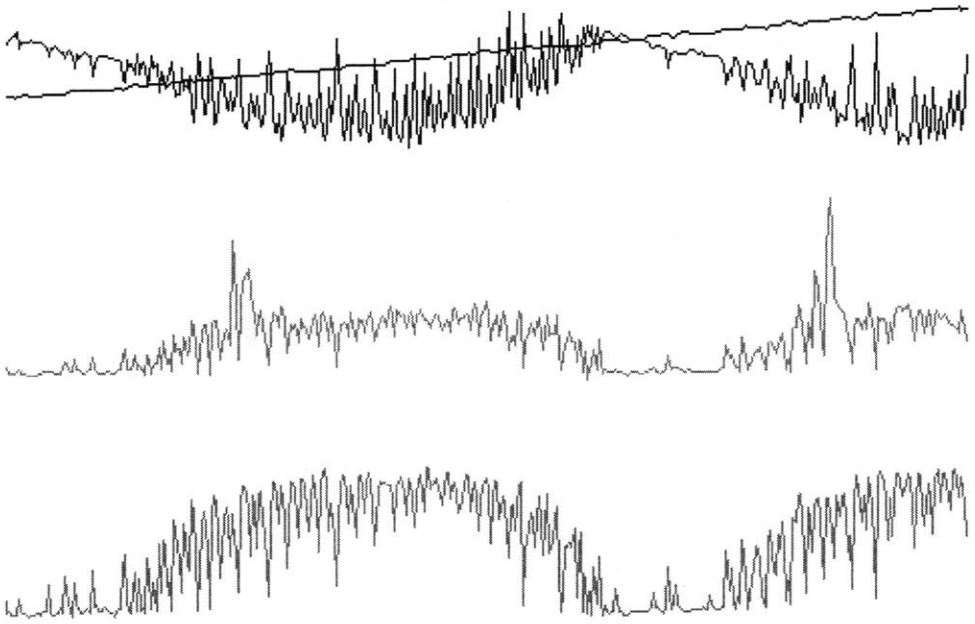

Figure 3-18: OPO behavior during a cavity length scan. From top to bottom: the upward sloped line is the PZT voltage corresponding to the cavity length change of 250 nm, the pump power showing weak resonance, the signal and the idler clusters. The crystal temperature is T=173°C. The appearance of signal and idler clusters is due to the conventional primary OPO, however the amplitude spike seen on the signal is probably due to the frequency doubled idler. This behavior does not imply divide-by-3 operation and phase locking.

generation was established, we proceeded to adjust the temperature, crystal position and beam parameters in order to find the signatures of phase locked operation. We expected to observe broadening of certain mode pairs as the cavity was scanned due to increased optical feedback as the divide-by-3 point was approached. In fact we observed what appeared to be mode broadening of the signal and idler at 173°C as shown in Figure 3-21; however, we have not been able to reproduce this behavior after the initial observation.

Further exploring the system behavior we noticed that beginning at ~155°C and up to ~185°C a prominent spike appears on the signal as seen in the middle trace

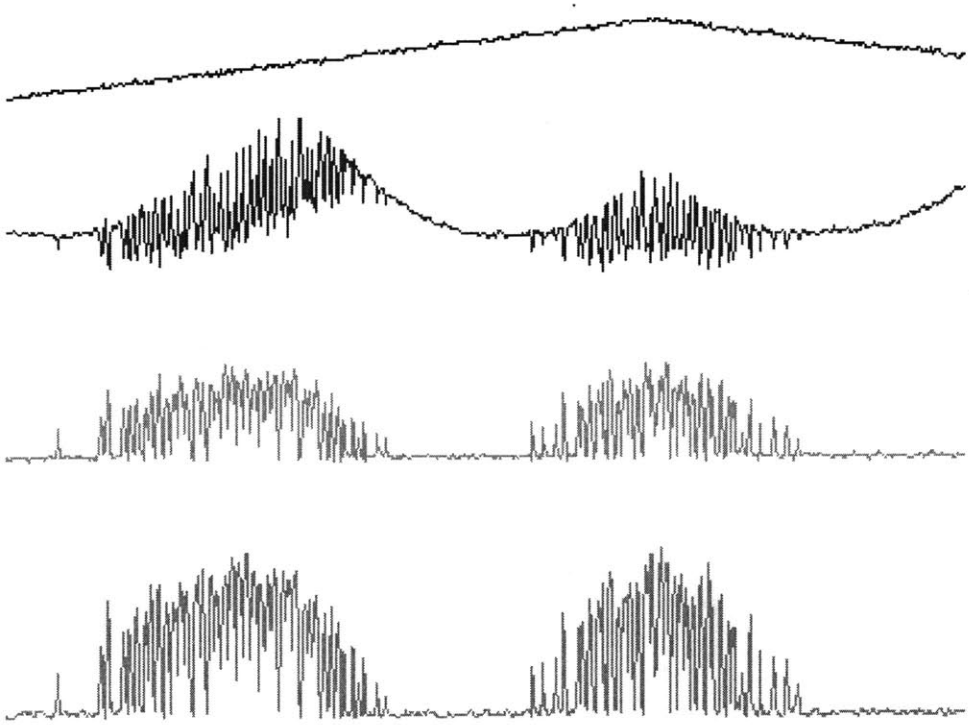

Figure 3-19: Conventional OPO behavior at T=180°C. The traces from top to bottom are: the cavity length scan with the full saw-tooth corresponding to cavity length change of 250 nm, the output pump power, the signal clusters and the idler clusters, respectively.

in Figure 3-18. The maximum amplitude of the spike can be as high as 5 times above the average signal level without any corresponding feature in the idler. The location of the spike within the cluster is dependent on the temperature, and the crystal position along the z-axis, which suggests to us that there may be a significant temperature gradient in that direction. The amplitude spike persists throughout the entire height (y-axis) of the crystal. It is difficult to speculate about the meaning of this observation until we perform further tests on the cavity mirrors and measure the finesse at the 800-nm signal wavelength in addition to the previous measurement at 1600 nm, both with and without the crystal. It is possible that the spike is not a signal mode from the primary OPO, but rather the frequency doubled idler, but without knowing the relative losses or the spectral content at the signal and idler wavelengths this behavior is difficult to explain.

As we increased the temperature further, between ~185°C and continuing to at

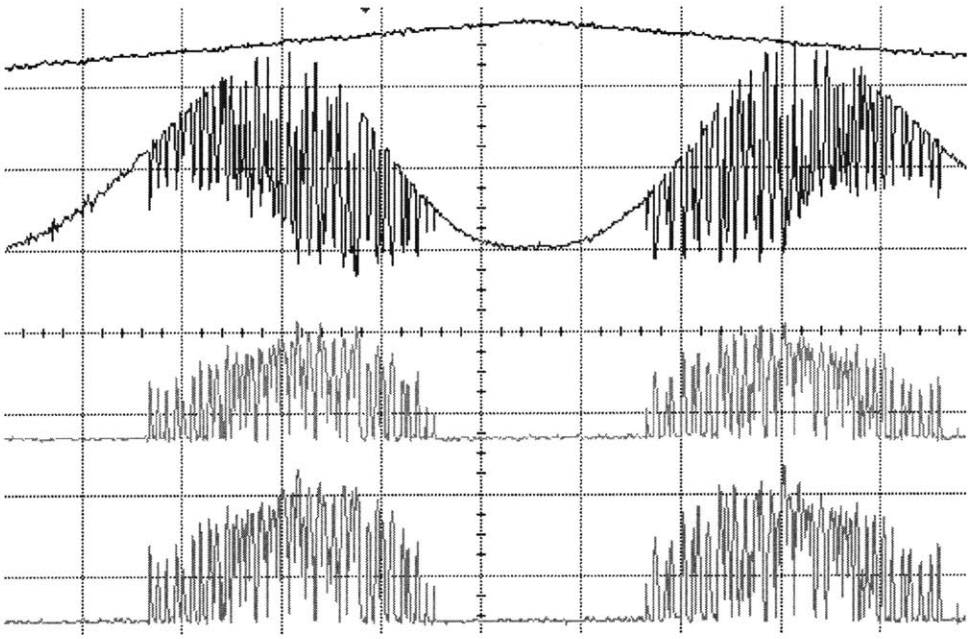

Figure 3-20: Conventional OPO behavior at T=205°C. The traces from top to bottom are: the cavity length scan, the output pump power, the signal clusters and the idler clusters, respectively.

least ~210°C (which is substantially higher than where we would expect phase locked operation to occur) signal clamping was observed, as shown in Figure 3-22. The idler exhibited an intensity dip whose position within the cluster was very sensitive to temperature, and would move from one edge of the cluster to the other as the temperature was tuned by ~ 1°C. At some temperatures within this range we noticed several plateaus at the signal output as shown in Figure 3-23. The signal behavior in the previous two figures is substantially different from the idler behavior, unlike the nearly perfect correlation that we had seen at lower temperatures.

We believe that the distinctive flattening of the signal output is characteristic of a secondary OPO pumped by the signal field of the primary OPO. At the higher operating temperatures the SHG section may allow proper phase matching for down conversion pumped by the signal output of the primary OPO to occur. This clamping is exactly the same behavior as seen in conventional OPOs operating above threshold including our own 532-nm pumped primary OPO system. As the input power was reduced we noticed that the signal clamping would disappear and normal signal and idler clusters were seen. Based on a rough calculation of the detected power (~100

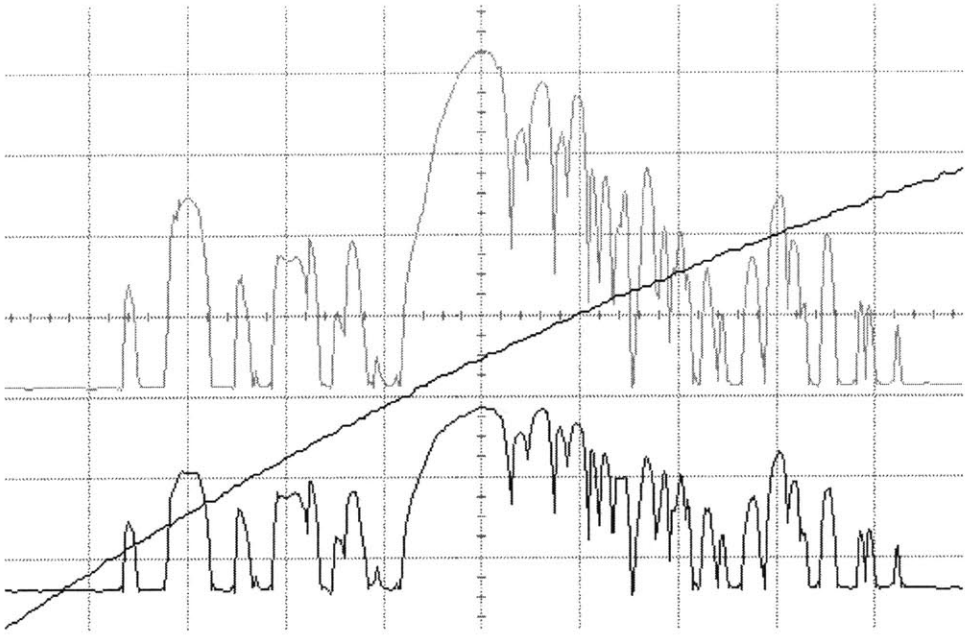

Figure 3-21: A single cluster scan. Mode broadening is seen on both outputs at 173°C. The curved saw-tooth is the PZT cavity scan voltage, and its shape is due to the low input impedance setting on the oscilloscope.

μW out of the cavity) and some assumptions about the output coupler cavity mirror (cavity finesse of ~1000) the threshold for the secondary OPO is estimated to be 100 mW. This number is almost identical to the threshold power for the primary OPO, but this is not surprising because the effective length of the OPO section is almost the same as the length of the SHG section.

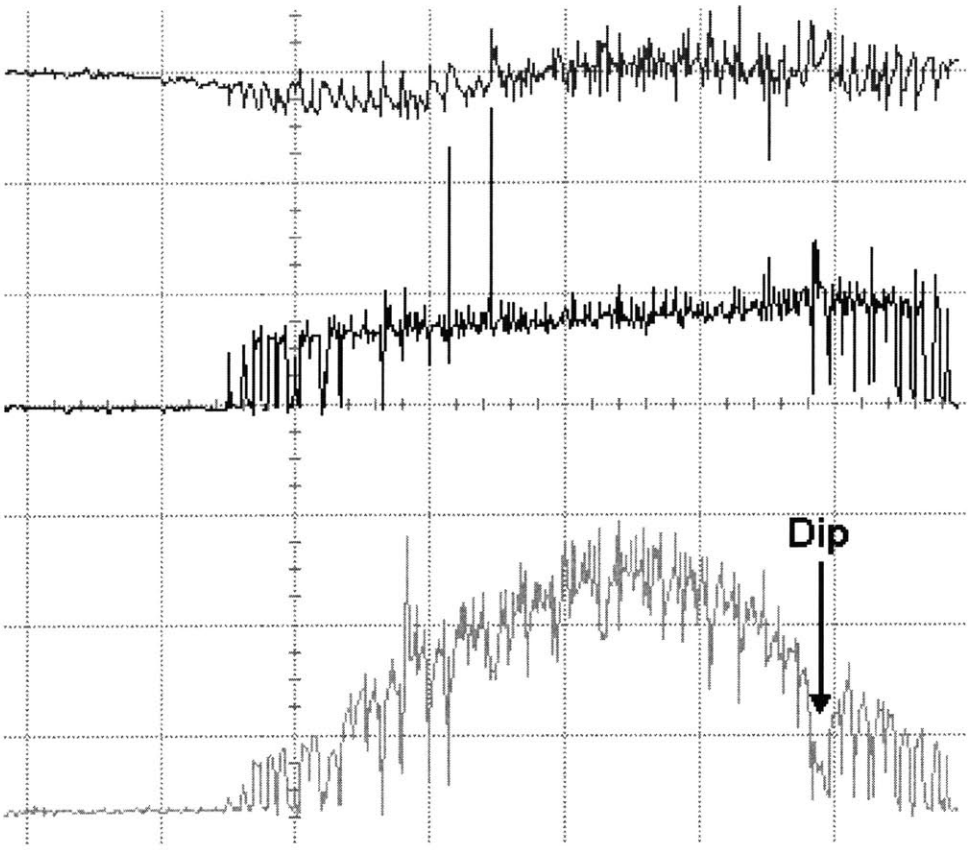

Figure 3-22: Operation at $\sim$ 205°C. The top trace shows the nearly flat pump; the second trace is of the clamped signal, and the lowest trace is the idler with an intensity dip that is highly temperature dependent. No direct correlation is seen between the signal and the idler as was observed earlier; however, it is apparent that the signal behavior changes as the idler intensity dip occurs. This behavior persists as the temperature is changed and the location of the dip moves through the cluster.

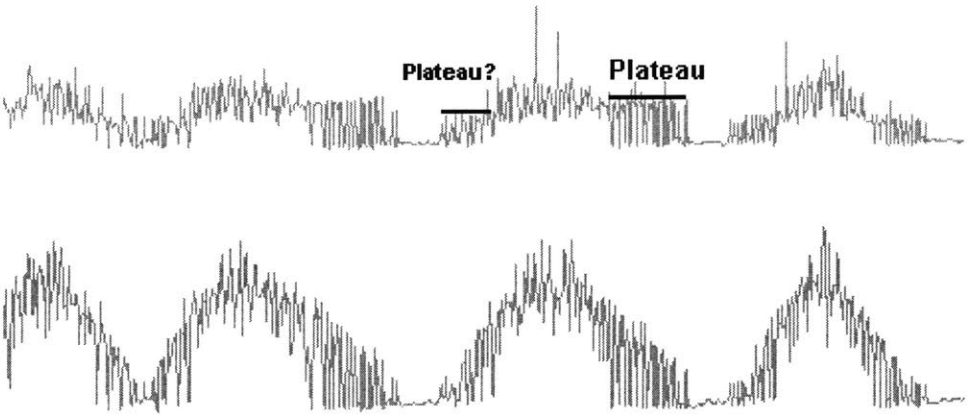

Figure 3-23: Several plateaus on the signal trace (top) but not on the idler (bottom) at T=207°C.

Chapter 4

Conclusion

4.1 Summary of Results

We have obtained preliminary results and characteristic signatures from our dual section OPO-SHG system and are currently working on exploring its behavior and attempting to achieve an optically self-phase-locked frequency divider. To do this we had to calculate the poling periods for the dual grating PPLN crystal to temperature match the two nonlinear processes, characterize the crystal by checking its effective nonlinear coefficient and the anti-reflection coatings, calculate the required threshold pump power, design and build an optical cavity and properly align it to allow the SPL OPO to function.

We have observed several types of behavior in our system corresponding to different operating regimes. We have seen characteristic mode broadening as the cavity length is scanned, which suggests that we have attained, at least temporarily, SPL operation. We have detected a peak at the signal wavelength which we believe to be an intense frequency doubled idler wave. We have also seen signal clamping that is very persistent with respect to temperature and crystal position changes. We attribute this last effect to an internally pumped secondary OPO. To the best of our knowledge this behavior has not been directly observed before.

We discovered several problems with the current setup. Our detection system is not yet sophisticated enough to fully understand the behavior of the system. We

also did not perform enough characterization of the cavity mirrors, which prevents us from adequately understanding some of phenomena that we have observed because depending on the reflectivity bandwidth certain cascading effects may or may not be possible. The single pass characterization that we performed using the Super Optronics oven is apparently not sufficient for the current system. The new oven seems to behave differently (worse) by allowing too much convective heat loss and producing a temperature gradient in the crystal. Due to this we are unsure where in the broad system temperature spectrum to look for self-phase locking.

4.2 Future Work

This experiment will continue along two primary paths. We will explore the cascaded OPO behavior where the signal wave from the primary OPO pumps the secondary OPO resulting in signal clamping that we have seen. We will also look for additional signatures of the signal-idler phase freezing, but before we proceed along this direction we will need to characterize our setup in a more accurate manner. Specifically, we will need to compensate for the poor oven design and repeat the single pass measurement to determine the proper operating temperature. We will also have to characterize the cavity at the signal and idler wavelengths with the crystal inside to be able to determine the relative losses. This would also allow us to investigate the behavior of Hopf bi-stabilities at pump powers greater than 4 times P_{th} which was the limiting case in Ref. [12]. In order to do this we will need to implement additional diagnostic equipment such as a Fabry-Perot cavity at the output of our OPO and possibly a frequency doubling crystal to verify the 3:1 behavior of our system in a direct manner. To this point the cavity has not been stabilized with a servo system; thus in order to obtain long term stability it will be necessary to design and build a side-lock servo mechanism that adjusts the cavity length via the PZT to maintain resonance in spite of mechanical/acoustical perturbations, temperature fluctuations and pump frequency drift.

Appendix A

A Brief Overview of Frequency Measurement Methods

As stated in Section 1.1 there is substantial motivation to be able to measure optical frequencies accurately. However, there are no optical frequency counters. Therefore it has been necessary to build bridges between the primary cesium (Cs) standard and the secondary standards implemented in the optical range. The current primary standard has a lot of technologies directly associated with it such as GPS and telecom; it has been tested and maintained over several decades in many facilities around the world. With continual improvement the Cs clock remains the primary frequency standard in which reproducibility is a major requirement. Thus any new standard must pass the reproducibility test over an extended period of time (in years or decades). However, it is becoming clear that for many of the emerging technologies higher resolutions and accuracies than those afforded by the Cs clock are becoming highly desirable. Moreover, the same fractional uncertainties can be reached in measurement times that are orders of magnitude faster in the optical regime than with the Cs clock. Furthermore, many of the secondary standards have higher resolutions than the primary standard that is used to calibrate them. These trends make it clear that with the shift of measurement and communication technologies, as dictated by the need for higher accuracies, toward the optical range, a new primary standard in the optical range will eventually replace the current cesium clock. To date, this optical clock is

still far from becoming reality, though many significant steps have been taken toward its development. As discussed in Chapter 1 femtosecond (fs) mode-locked laser based optical frequency combs that span an octave or more have become the best method to accurately measure optical frequencies relative to the Cs clock without the need for direct optical frequency counting. The ability to connect optical and microwave frequencies is a significant step toward realizing an optical primary frequency standard. This appendix gives a cursory overview of some of the technologies that emerged and have since given way to the comb.

A.1 An Ideal Optical Clock

Before I describe the previous approaches to optical frequency counting it is beneficial to provide an idea of where the field would like to go. An ideal optical clock is a device that undergoes very stable transitions and a system that is capable of counting these transitions. A clock with higher transition rate will have better temporal resolution; however, in order for it to become a frequency standard the transition rate must be maintained with very low and limited drift over a long period of time.

The ideal way to distribute the optical clock frequency would be a stable, accurate, stand-alone comb with evenly spaced, absolutely determinable frequency markers linked to the clock. The spacing between adjacent markers should be small enough to be measured directly using standard heterodyne measurement and subsequent microwave frequency measurement techniques. The comb should cover a significant portion of the optical spectrum, i.e., from the ultraviolet to the far infrared. With such a system any unknown optical frequency could be measured by performing a beat measurement against the closest frequency marker. The frequency markers must have enough power to enable the beat measurement to be performed easily and to enable phase locking of additional systems. This clock system must be easily reproducible and must exhibit higher precision, accuracy and stability than the current primary frequency standard and current time distribution system. Even though the optical clock is not a reality yet, various subsystems that would make this clock feasible have

been designed, implemented and tested. It has been suggested that such a clock may be stable to ± 1 s in 4 billion years, or roughly 1 part in 10^{17}.

The next several sections describe the primary standard as well as several secondary standards that have been shown to have higher accuracies than the current clock. Various technologies to connect them to the current primary standard will be introduced, and the femtosecond mode locked laser comb will be shown to be an ultimate, for the time being, method of bridging the frequency gap.

A.2 Primary Microwave Frequency Standard

The primary standard is a clock whose stability has been confirmed in many laboratories and verified over a long time scale. At the beginning of the 20th century when frequency metrology was in its infancy the primary oscillator was based on an LC circuit. It was soon replaced with a quartz oscillator, and then with an atomic standard in the late 1940s. The current primary frequency standard is a cesium-133 atomic clock oscillating at 9.2 GHz on a hyperfine transition of the ground state. The precise definition of the second that was adopted in 1968 and is still in use is "the duration of 9 192 631 770 periods of the radiation corresponding to the transition between the two hyperfine levels of the ground state of the Cesium 133 atom." [35]. This definition is valid for an atom at rest at 0 K. Therefore the real frequency used to define the second must be corrected for the perturbative effects of the ambient radiation. In principle, as a primary standard, it should be the most stable standard and be used for generating and calibrating secondary standards. An overview of the development of atomic clocks is given in [43] and [46]

There are several metrics that are used to describe the quality of a frequency standard. These are: accuracy, precision and stability. Accuracy is the deviation between the result of a measurement and the "true" value. Since the primary standard is used to define the "true value" of a unit of time it is by definition and by design very accurate. The accuracy can be checked by its reproducibility in different clocks operating at different locations. Precision is a measure of the intrinsic (not relative to the true

Table A.1: Comparison of frequency standards

Name	CSU	Notes
Agilent 5071	$5 * 10^{-13}$	Commercial Product
NIST-7	$5 * 10^{-15}$[44]	Atomic standard utilizing a thermal beam of Cs atoms
NIST-F1	$1.5 * 10^{-15}$[45]	Fountain atomic standard. Utilizes optical mollasses to increase interaction time with probing microwave radiation, thereby reducing uncertainty

value) statistical spread of measurements taken at different times. Note that a precise measurement does not imply the same level of accuracy if there are perturbations that prevent the measurements from being reproducible over time. Stability is the metric of isolation of the output of the standard with respect to the external environment and its effects manifested through vibrations, temperature fluctuation, radiation, etc. According to these definitions devices that are chosen to be the primary standards must exhibit high accuracy, precision and stability. It should be noted that even the primary standards are continuously being evaluated and cross checked with primary standards at other locations. A frequently used measure to determine the quality of a primary standard is the Combined Standard Uncertainty (CSU). The CSU incorporates statistical fluctuations between many consecutive measurements, as well as the sum of the uncertainties due to external biases. The CSU is a practical measure of how well a particular standard implements the definition of the second and is defined as $\Delta\nu/\nu_0$ [44]

A.3 Secondary Optical Frequency Standards

For practical work in the optical frequency range, secondary standards have been established to be used as easy references. These standards such as the I_2 stabilized HeNe laser at 633 nm, the CH_4 stabilized HeNe laser at 3.39 μm and OsO_4 stabilized CO_2

among many others, have been measured against the primary standard with a conventional microwave to optical frequency chain [47]. More recently optical secondary standards such as those that rely on RF trapped ions [37], magneto-optically trapped atoms [38], and narrow line-width molecular transitions [39] have been implemented. It is now possible to stabilize lasers to these narrow atomic or molecular transitions, and these advancements make it possible to build optical frequency standards. They already show stabilities that are much higher than the current primary standard, with the potential to improve accuracy by several orders of magnitude over the primary cesium source. Resolution near 10^{-16} has already been demonstrated [36]. However, all of the aforementioned secondary standards have to be calibrated with respect to the primary standard because their long term stability has not been sufficiently verified. Since there were no direct methods for measuring optical frequencies, techniques to bridge the frequency gap became necessary [41]. Furthermore, these secondary standards are not always available in the region of the spectrum where a measurement needs to be made.

The precision gained by utilizing a novel secondary standard cannot be fully exploited when it is linked to the primary Cs standard, and the system accuracy is still limited by the accuracy of the atomic clock. It is therefore imperative to develop techniques that will enable the optical standards to become the new primary standards. When they are realized, these optical clocks will substantially improve frequency measurement resolution with hopes of attaining accuracies on the order of few parts in $10^{17} - 10^{18}$.

A.4 Microwave to Optical Frequency Chain

The traditional approach to provide a link over the 5 orders of magnitude in frequency between the primary microwave and secondary optical standards, has been to utilize complex frequency chains comprising complicated arrays of phase locked diode lasers, CO_2 IR lasers, masers and other microwave oscillators coupled through nonlinear devices to realize phase coherent frequency multiplication, frequency synthesis or

frequency division schemes [33]. An example of a phase coherent frequency chain linking a secondary Ca optical standard to the primary standard is shown in Figure A-1 [33]. These chains have been documented extensively in literature and their overview is given in Ref. [34]; however, they have proved to be difficult to implement in practice and are not available for commercial use because they require a laboratory of equipment and personnel to maintain them. Alternative and superior techniques of allowing frequencies in the range of hundreds of THz to be measured via so called "all optical methods" have become popular in the last decade and a half.

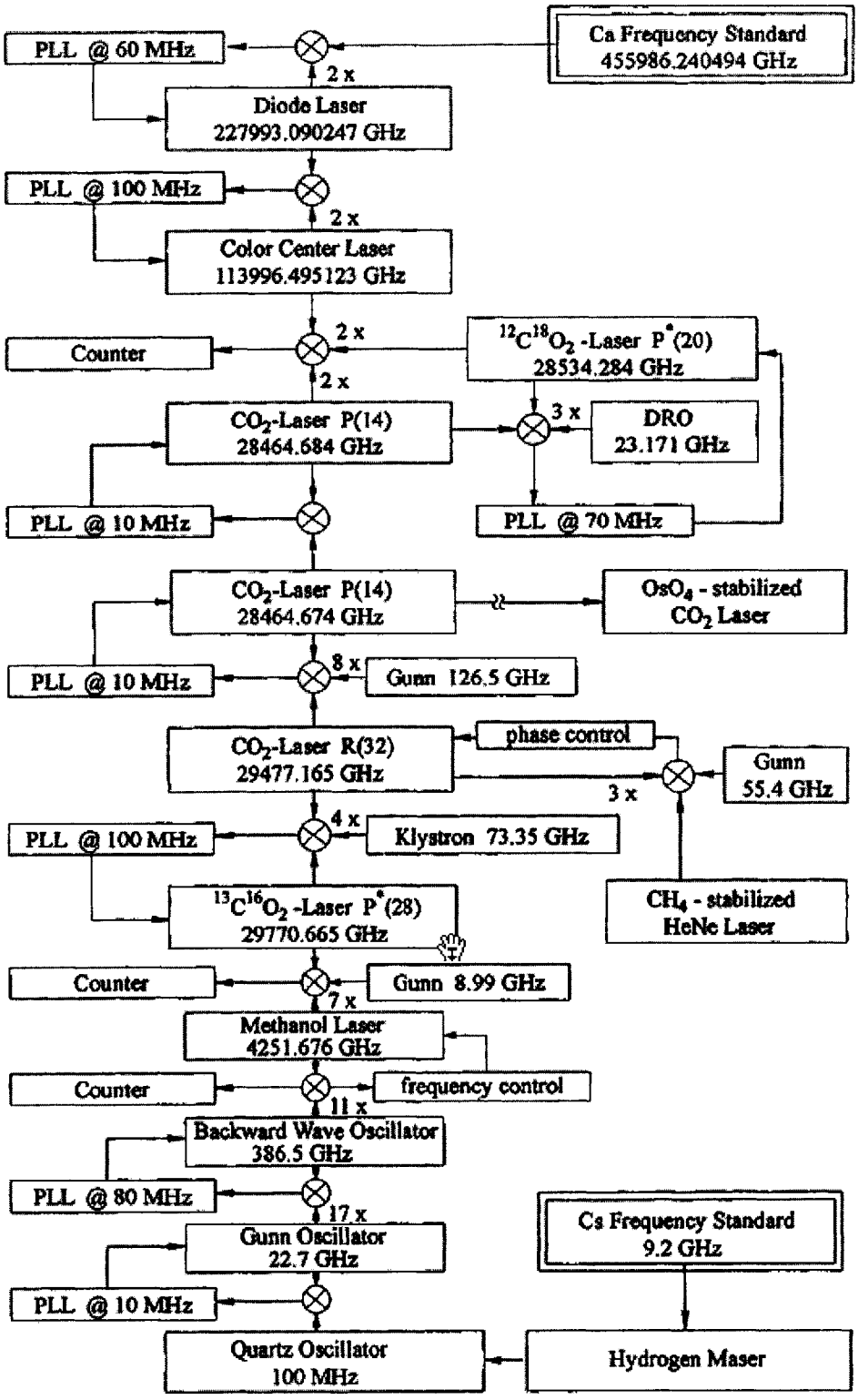

Figure A-1: Frequency chain for linking the Ca optical frequency standard to the Cs clock [33].

A.5 Optical Frequency Scaling, Series Approach

In 1990 Telle, *et al* proposed phase coherent frequency division by exactly halving the frequency difference of two lasers. This was accomplished by phase locking the second harmonic of a third laser to the sum frequency of the first two. The frequency of the third laser is exactly locked at the midpoint of the two input frequencies [40]. By repeated application of this method where one input frequency carries over from stage to stage and the second input to stage $n+1$ is the output of stage n, optical frequency differences can be repeatedly divided. Systematic application of this technique will reduce the difference frequency to the microwave range where it can be directly measured. As described, this system only provides a *difference* frequency measurement; however, if the two original input frequencies have a specific frequency relationship (e.g., one is the second harmonic of the other), then an absolute frequency measurement can be made. The main advantage of this method is that it does not measure the absolute frequency directly, thus only optical and near IR lasers are utilized even though radio frequency precision is obtained. The clear disadvantage of this system is that very high pump powers are necessary to pump the multiple nonlinear generating steps. This technique was utilized in [4] to determine the stability of mode-locked laser combs where it was also shown that it was possible to perform measurements of frequencies separated by as much as 20 THz, thus reducing the number of series stages necessary.

A.6 Frequency Comb, Parallel Approach

A technique that elaborates on the above idea was introduced by Wong in 1992 [41]. He proposed that instead of repeatedly dividing an optical frequency f until it can be measured in the GHz range, the value of f can be determined by measuring the difference frequency between two integral subharmonics of f. The system consists of a stable laser that is used to pump two master optical parametric oscillators and N auxiliary OPOs that are parallel with each other and phase-locked together. The

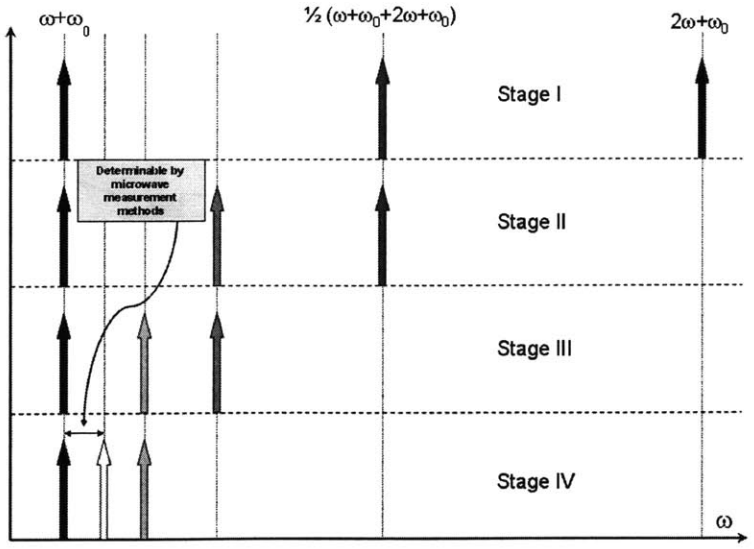

Figure A-2: Several OPOs in series halve the frequency at each stage until it can be measured with conventional methods. The lighter shades indicate reduced power in the consequent stages.

end result is that the pump f is split into an ultrawideband comb of phase coherent frequencies that span the range from $1\mu - 2\mu$. One of the comb spacings is phase locked to a microwave frequency which means that every frequency marker of the comb is fully characterized. With this setup an unknown frequency can easily be determined by performing a beat measurement against the nearest comb marker. The advantages of this approach are that this technique is all-optical; it eliminates the complicated frequency chain and the inherent frequency uncertainty is limited by the pump line width and the OPO phase diffusion; it produces a very broad frequency comb with measurement and synthesis capability between $.4 - 0.7\mu$m. The disadvantage of this system is in its difficulty of implementation. It relies on multiple OPOs and is likely to be almost as complicated as the frequency chain that it attempts to replace.

A.7 Femtosecond Comb

With the realization of octave spanning optical combs based on mode-locked femtosecond lasers the possibility of building a convenient secondary optical standard has come closer. A pulsed laser with short pulse length and periodic pulse spacing

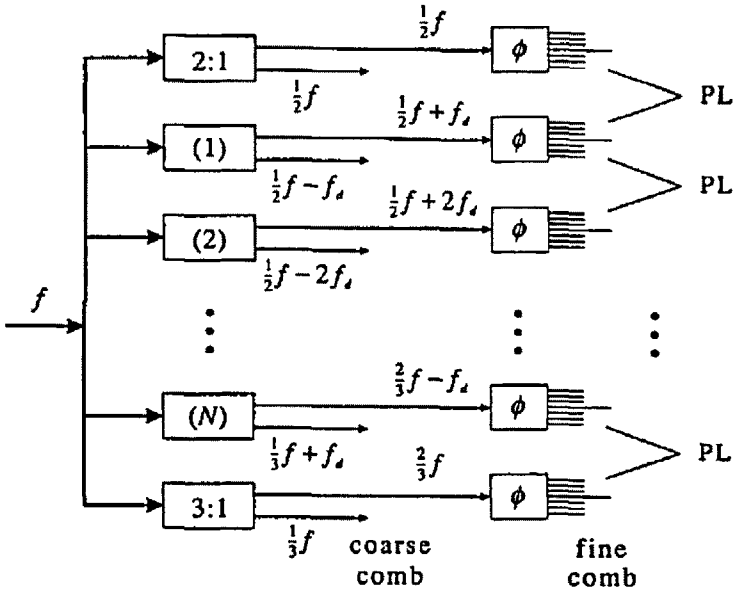

Figure A-3: A parallel configuration of OPOs that would theoretically enable an optical comb to be generated [41].

necessarily contains an array of evenly spaced frequencies. It was shown that the stability of these comb elements is excellent [4]. A fs laser is based on the Kerr lens mode-locking effect, where due to a nonlinearity (usually in the gain medium itself) the index of refraction is intensity dependent. It focuses higher intensity modes more than the lower intensity modes. Combined with an internal aperture this allows the high intensity (short) pulses to pass through the aperture while eliminating the lower intensity, longer, less focused pulses. By this method only the shortest and highest intensity pulses survive, resulting in an ultrashort-pulse mode-locked pulsed laser. The pulse length is inversely proportional to the medium gain bandwidth, so the more modes are present the shorter the pulse is, thus the Ti:Sapphire laser with its broad gain profile is well suited for generating very short pulses.

As seen in the previous few paragraphs there are several methods that have potential for bridging the gap between the optical frequencies of interest and the microwave frequencies that can be directly measured. However the methods clearly vary in complexity of implementation and practical usability. The technique that will eventually become an accepted method to accurately and precisely measure optical frequencies

must overcome the problems associated with previous methods and it must have certain characteristics that would make it appealing. It must

- Cover a broad range of frequencies spanning from UV to far IR;
- Require a small number of subsystems to operate;
- Be stable over long time scales, and
- Have greater or equal precision than the primary atomic standard

At this time it appears that a system relying on an optical comb based on a femtosecond pulsed mode-locked laser is the simplest and most direct way to meet the above criteria.

Appendix B

Cavity Design 3 Views

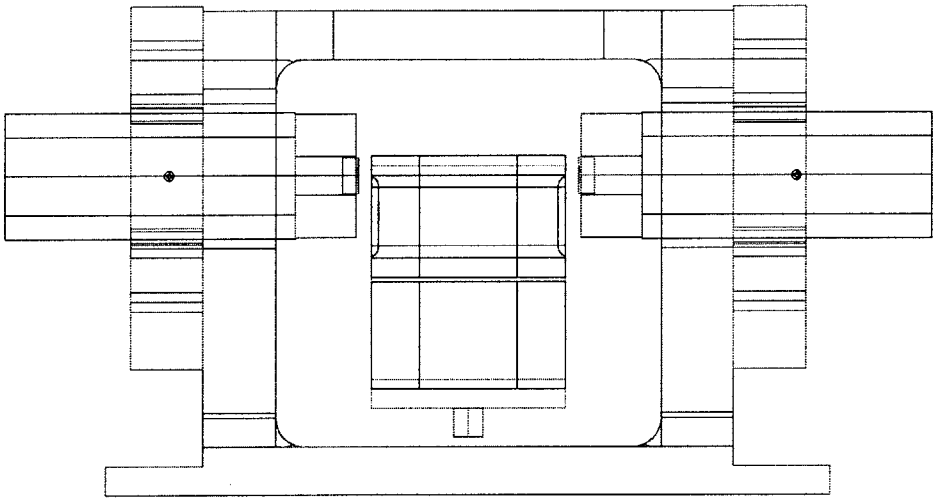

Figure B-1: 2-D front view.

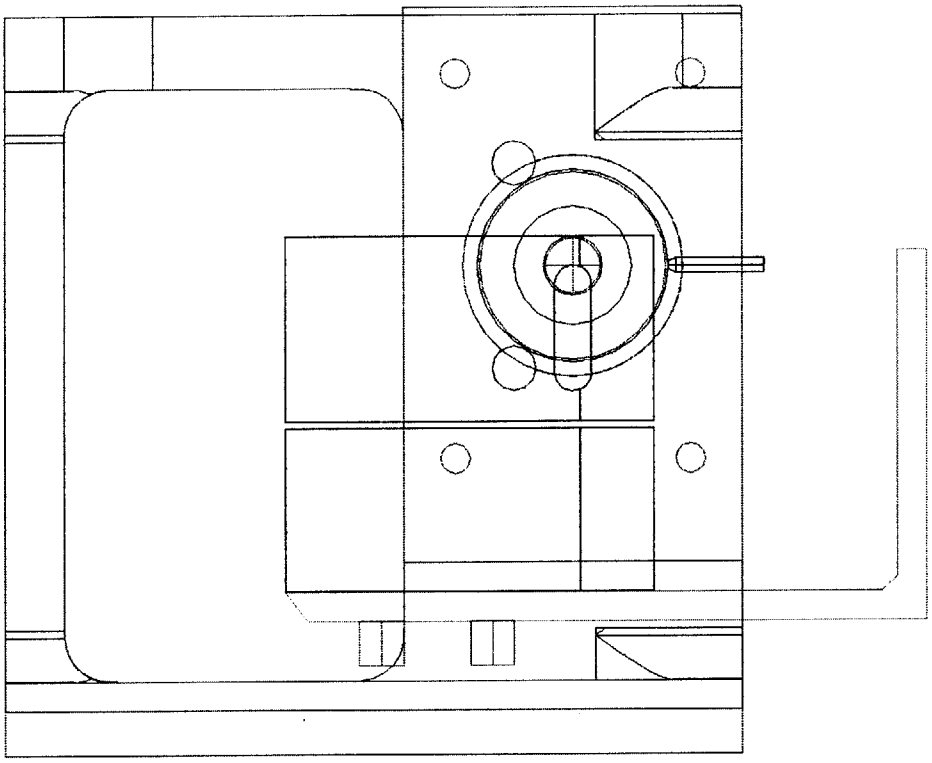

Figure B-2: 2-D side view.

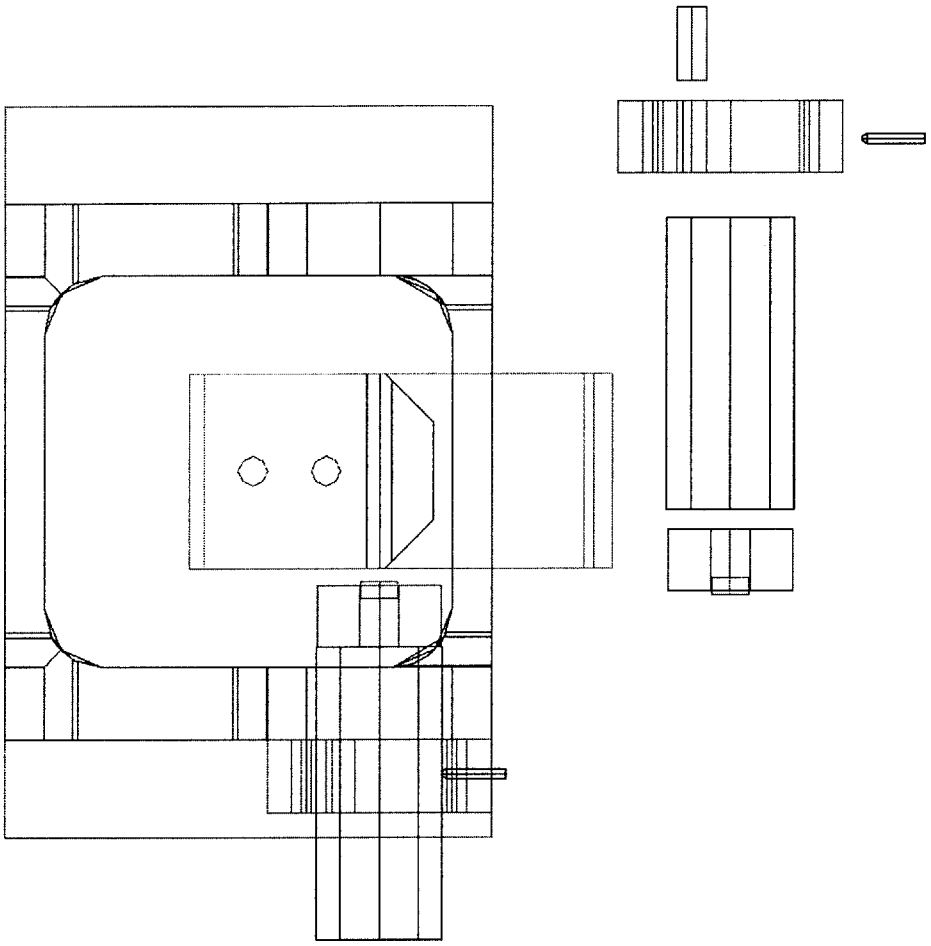

Figure B-3: 2-D top view.

Bibliography

[1] D. B. Sullivan *et. al. Journal Res. National Institute of Standards and Technoly*, **106**, 47 (2001).

[2] C. Schwob, et al., *Physical Review Letters* **82**, 4960 (1999).

[3] Th. Udem, J. Reichert, R. Holzwarth, T. W. Hansch, *Physical Review Letters*, **82**, 3568 (1999).

[4] Th. Udem, J. Reichert, R. Holzwarth, T. W. Hansch, *Optics Letters*, **24**, 881 (1999).

[5] D. E. Spence, P. N. Kean, W. Sibbett, *Optics Letters*, **16**, 42 (1990).

[6] S. A. Diddams *et. al. Physical Review Letters*, **84**, 5102 (2000).

[7] R. Ell, U. Morgner, F. X. Kartner, J. G. Fujimoto, E. P. Ippen, V. Scheuer, G. Angelow, T. Tschudi, M. J. Lederer, A. Boiko, B. Luther-Davies, *Optics Letters*, **26** 373 (2001).

[8] D. H. Lee "Phase-Coherent by-three-division of a diode laser frequency with an optically self-phase-locked continuous-wave optical parametric oscillator.", Universitat Kaiserslautern, (2000).

[9] P. T. Nee "Optical Frequency Division via Periodically-Poled-$LiNbO_3$-Based Nonlinear Optics", MIT, (1999).

[10] J. J. Zondy, A. Douillet, *Physical Review A*, **63**, 023814 (2001).

[11] J. J. Zondy, *Physical Review A*, **67**, 035801 (2003).

[12] J. J. Zondy, D. Kolker, N. C. Wong, *Physical Review Letters*, **93**, 043902 (2004).

[13] A. Yariv, Optical Electronics in Modern Communications, Oxford University Press, New York, NY, (1997) pp. 273-282

[14] M. L. Bortz, M. L. Arbore, M. M. Fejer, *Optics Letters*, **20**, 49 (1995)

[15] M. M. Fejer, G. A. Magel, D. H. Jundt, R. L. Byer, *IEEE Journal of Qunatum Electronics*, **28**, 2631 (1992).

[16] L. E. Myers, *et al*, *Journal of Optical Society of America B*, **12**, 2101 (1995).

[17] M. Yamada, N. Nada, M. Saitoh, K Watanabe, *Applied Physics Letters*, **62**, 435 (1993).

[18] W. K. Burns, W. McElhanon, L. Goldberg, *Photonics Technology Letters*, **6**, 252 (1994).

[19] D. H. Jundt, *Optics Letters*, **22**, 1553 (1997).

[20] R. Graham, H. Haken *Zeitschrift fur Physik*, **210**, 276 (1968).

[21] D. Lee, N. C. Wong, *Journal of Optical Society of America*, **10**, 1659 (1993).

[22] E. J. Mason, N. C. Wong, *Optics Letters*, **23**, 1733 (1998).

[23] N. C. Wong, *Physical Review A*, **45**, 3176 (1992).

[24] A. E. Siegman, *Lasers*. University Science Books, Sausalito, CA., 1986

[25] M. Vaidyanathan, R. C. Eckardt, V. Dominic, L. E. Myers, T. P. Grayson, *Optics Express*, **1**, 49 (1997).

[26] R. C. Eckardt, C. D. Nabors, W. J. Kozlovsky, R. L. Byer, *Journal of Optical Society of America B*, **8**, 646 (1991).

[27] I. Shoji, T. Kondo, A. Kitamoto, M. Shirane, R. Ito, *Journal of the Optical Society of America B*, **14**, 2268 (1997).

[28] P. Meystre and M. G. Moore. *Directions in Quantum Optics*, Springer-Verlag, 116 (2001).

[29] http://www.hcphotonics.com

[30] H. Kogelnik, T. Li, *Applied Optics*, **5**, 1550 (1966).

[31] G. D. Boyd, D. A. Kleinman, *Journal of Applied Physics*, **39**, 3597 (1968).

[32] B. Lai, N. C. Wong, L. K. Cheng, *Optics Letters*, **20**, 1779 (1995).

[33] Schnatz *et al., Physical Review Letters* **76**, 18 (1996).

[34] G. D. Rovera, O. Acef, *Topics in Applied Physics*, **79**, 249, Springer-Verlag (2001).

[35] National Physical Laboratory, http://www.npl.co.uk

[36] M. G. Major. *The Quantum Beat: The Physical Principles of Atomic Clocks.* Springer-Verlag, (1999).

[37] E. Peik, G. Hollemann, H. Walther. *Physical Review A*, **49**, 49 (1994).

[38] H. Schnatz, B. Lipphardt, J. Helmcke, G. Zinner. *Physical Review Letters*, **76**, 18 (1996).

[39] P. Junger, S. Swartz, M. Eickhoff, J. Ye, J. L. Hall, S. Waltman. IEEE *Transactions on Instrumentation and Measurement*, **44**, 151 (1995).

[40] H. R. Telle, D. Meschede, T. W. Hansch, *Optics Letters*, **15**, 532 (1990).

[41] N. C. Wong, *Optics Letters*, **17**, 1155 (1992).

[42] D. H. Lee, M. E. Klein, J. P. Meyn, P. Grob, R. Wallenstein, K. J. Boller, *Optics Express*, **5**, 114 (1999).

[43] R. E. Beehler, *Proceedings of IEEE*, **95**, 792 (1967).

[44] J. H. Shirley, W. D. Lee, R. E. Drullinger, *Metrologia*, **38**, 427 (2001).

[45] S.R. Jefferts, J. Shirley, T.E. Parker, T.P. Heavner, D.M. Meekhof, C. Nelson, F. Levi, G. Costanzo, A. De Marchi, R. Drullinger, L. Hollberg, W.D. Lee, F.L. Walls, *Metrologia*, **39**, 321 (2002).

[46] N. F. Ramsey, *Journal Res. National Bureau of Standards*, **88**, 301 (1983).

[47] T. J. Quinn. *Metrologia*, **36**, 211 (1999).